Intracontinental deformation and volcanism in the Hangai and Gobi-Altai Mountains in Mongolia: Insights from a magnetotelluric multiscale 3-D inversion

J.S. Käufl[1*], A.V. Grayver[1], M.J. Comeau[2], A.V. Kuvshinov[1], M. Becken[2], J. Kamm[23], E. Batmagnai[1], S. Demberel[4]

[1] *Institute of Geophysics, Department of Earth Sciences, ETH Zürich, Switzerland*

[2] *Institut für Geophysik, WWU Münster, Germany*

[3] *Geological Survey of Finland, Espoo, Finland*

[4] *Institute of Astronomy and Geophysics, Mongolian Academy of Sciences, Ulaanbaatar, Mongolia*

[*] *Corresponding author, Email: johannes.kaeufl@erdw.ethz.ch*

11 October 2019

Summary

Central Mongolia is a prominent region of intraplate volcanism and surface deformation. To study these processes, which are poorly understood, we collected magnetotelluric data in the Hangai and Gobi-Altai region in central Mongolia and derived the first three-dimensional resistivity model of the crustal and upper mantle structure in this region.

The geologic history of this region is complex, resulting in features over a wide range of spatial scales, which are coupled through a variety of geodynamic processes. Three-dimensional imaging using magnetotellurics can resolve the distribution of electrical conductivity within the Earth at scales ranging from tens of metres to hundreds of kilometres. However, designing a survey which can probe various scales and running subsequent three-dimensional inversions requires that multiple constraints imposed by the data acquisition cost, logistical efforts and computational complexity are satisfied.

We present an approach to survey design, data acquisition, and inversion that aims to bridge various spatial scales while keeping the required field work and computational costs feasible. Magnetotelluric transfer functions were estimated for a 650×400 km^2 grid, which included measurements on an array with regular 50×50 km^2 spacing and along several profiles with a denser 5-15 km spacing. The use of telluric-only data loggers on these profiles allowed for an efficient data acquisition with a high spatial resolution. A 3-D finite element forward modelling and inversion code was used to obtain the resistivity model. Locally refined unstructured hexahedral meshes allow for a multi-scale model parametrization and accurate topography representation. The inversion process was split into four stages whereby the result from each stage was used as input for the following stage, that included a finer model parametrization and/or additional data (i.e. more stations, wider frequency range).

The final model reveals a detailed resistivity structure and fits the observed data well across all periods and site locations, offering new insights into the subsurface structure of central Mongolia. A prominent feature is a large low-resistivity zone detected in the upper mantle that is attributed to partial melting within an asthenospheric upwelling that shallows to a depth of 70 km, consistent with previous studies. The first 3-D model reveals the complex

geometry of the upwelling, which appears rooted below the Eastern Hangai Dome with a second smaller upwelling southwest of the Hangai Dome.

Thanks to the multi-scale approach, the conductive signatures of late Cenozoic volcanic zones and modern geothermal areas can be traced throughout the crust and lithosphere and linked to the mantle upwelling. Other features of interest include well resolved, heterogeneous low-resistivity zones in the lower crust, a highly resistive upper crust throughout the Hangai, consistent with a cratonic block, and shallow, conductive sediments in the Valley of Lakes south of the Hangai Dome. Furthermore, the conductive signatures of several major fault systems were imaged, which accommodate the intracontinental deformation, mark terrane boundaries, and host the mineralized zones of the Bayankhongor Ophiolite Belt.

Key words: Magnetotellurics, Inverse theory, Numerical modelling, Electrical properties, Asia, Structure of the Earth

1 INTRODUCTION

Located deep in the continental interior, far away from plate boundaries, central Mongolia is a region of active intracontinental deformation (Calais et al. 2003; Walker et al. 2007, 2008) and young Cenozoic volcanism (e.g. Barry et al. 2003; Ancuta et al. 2018). With the stable Siberian Craton to the North, central Mongolia occupies the transition zone between the North-South compressional regime of the India-Asia collision and the eastward extension motion due to the Pacific subduction (Calais et al. 2003). This transition zone is dominated by the Hangai Dome, a low relief, intracontinental plateau elevated up to 2 km above the regional average (Cunningham 2001). It is bounded by large seismically active strike slip faults, which experienced large (Magnitude > 8) intracontinental earthquakes in the last century (Walker et al. 2007). Additionally, dispersed, low-volume, intraplate volcanism is observed during the last 35 Ma throughout central Mongolia (Barry et al. 2003; Hunt et al. 2012; Ancuta et al. 2018).

The cause of the volcanism and the mechanism of the Hangai Dome uplift remain enigmatic. In particular, the link between uplift and volcanism is an open topic of research. Some

63 authors argue for contemporaneous processes (e.g. Cunningham 2001; Sahagian et al. 2016),
64 whereas others claim that the uplift might have predated the volcanic activity (McDannell
65 et al. 2018).

66 Previous seismic and gravity studies of the region found a low velocity/low density
67 anomaly in the upper mantle below the Hangai confined to depths of $70-150$ km (Priestley
68 et al. 2006; Tiberi et al. 2008), and a low shear-wave velocity anomaly that possibly extends
69 to a depth of more than 410 km (Chen et al. 2015). A thick crust ($50-55$ km) and a shal-
70 low ($60-80$ km) lithosphere-asthenospere-boundary (LAB) was found by seismic studies
71 (Priestley et al. 2006; Petit et al. 2008) and is supported by the analysis of erupted xeno-
72 liths (Barry et al. 2003; Ionov 2002). Petrochemical analysis of erupted basalts and mantle
73 xenoliths estimates the melting source at depths of 70 to 150 km (Hunt et al. 2012; Barry
74 et al. 2003), in good agreement with the depth of the LAB and the low velocity/low density
75 anomalies.

76 This combined evidence is inconsistent with an earlier explanation for the intraplate
77 volcanism: a deep-rooted mantle plume (Windley & Allen 1993). More recent explanations
78 for the volcanism and uplift include crust-mantle interactions such as lithospheric thinning
79 (due to delamination, convective removal, or edge-driven convection) or asthenospheric flow
80 and dynamic topography (see Ancuta et al. 2018). However, a comprehensive explanation
81 is still missing, partly due to the lack of detailed three-dimensional (3-D) images of the
82 subsurface in the region. To obtain this information, we conducted a magnetotelluric (MT)
83 survey in the Hangai and Gobi-Altai region from 2016 to 2018.

84 Geological and geodynamic processes, such as the intracontinental deformation in Mon-
85 golia and asthenospheric upwelling, happen at a wide range of spatial scales. This motivated
86 us to design a MT survey and develop a 3-D inversion scheme that can consistently embrace
87 and bridge multiple spatial scales.

88 In practice, any survey design is often limited by the cost of data acquisition and the re-
89 quired logistical effort. Because a uniform, dense grid of sites can be prohibitively expensive
90 to collect, an attractive alternative is complementing a coarser, large-scale grid of sites with

more densely spaced sites in regions of primary interest. Furthermore, the cost and logistical efforts of a survey can be significantly reduced when using the Telluric-Magnetotelluric (T-MT) method (Hermance & Thayer 1975), whereby the magnetic field is recorded only at a subset of locations (Iliceto & Santarato 1986; Yungul 1977; García & Jones 2005; Melosh et al. 2010; Campanyà et al. 2014). From a methodological perspective, handling T-MT data requires only modest modifications of the data processing and inversion tools to take full advantage of simultaneously recording arrays (Egbert 2002). Both of these considerations were addressed during data analysis and inversion. For the three-dimensional interpretation of MT data collected at an observation grid of highly variable spacing, one needs an inversion strategy that provides sufficient flexibility in parametrizing the subsurface. This allows varying lateral and vertical resolution lengths to be appropriately accounted for without using an excessive number of unknown model parameters, which would impose additional computational constraints and increase non-uniqueness.

In this paper we focus on the methodological side of the problem and present an approach on how to bridge the different spatial scales in 3-D MT inversions, applied to the data collected in the Hangai and Gobi-Altai mountains in Mongolia. Implications regarding the Hangai uplift and volcanism, as well as regional geodynamics and geology, previously discussed by Comeau et al. (2018c) on the basis of a 2-D model from a subset of the data, are expand upon here with new insights from the 3-D resistivity model.

2 DATA

2.1 The magnetotelluric method

The MT method is a geophysical technique used to probe the conductivity structure of the Earth by using natural electromagnetic (EM) field variations (Rikitake 1948; Tikhonov 1950; Cagniard 1953). The Earth's response to external excitation is described by frequency-dependent transfer functions (TF), which carry information about the electrical conductivity distribution. We work with the magnetotelluric impedance tensor $\mathbf{Z}$, which links horizontal

electric and magnetic fields as:

$$\vec{E}_h(\omega, \vec{r}_l) = \mathbf{Z}(\omega, \vec{r}_l)\, \vec{H}_h(\omega, \vec{r}_l). \tag{1}$$

Here, ω is the angular frequency. $\vec{E}_h(\omega, \vec{r}_l) = (E_x, E_y)$ and $\vec{H}_h(\omega, \vec{r}_l) = (H_x, H_y)$ are the Fourier transforms of the horizontal components of the electric (E-) and magnetic (H-) fields at the location $\vec{r}_l$. Henceforth, the frequency dependence is implied and will be omitted for simplicity. H- and E-fields act as the input and output of the linear system described by the impedance

$$\mathbf{Z}(\vec{r}_l) = \begin{pmatrix} Z_{xx}(\vec{r}_l) & Z_{xy}(\vec{r}_l) \\ Z_{yx}(\vec{r}_l) & Z_{yy}(\vec{r}_l) \end{pmatrix}, \tag{2}$$

which is a second-order frequency dependent, complex-valued tensor. It carries the information about the 3-D electrical conductivity distribution σ in the earth. Instead of the conductivity, its inverse, the resistivity ($\rho = \sigma^{-1}$) can be used interchangeably. For each of the four tensor elements we can calculate the phase

$$\phi_{ij}(\vec{r}_l) = \tan^{-1}(Z_{ij}(\vec{r}_l)) \qquad \text{with} \quad i, j \in \{x, y\} \tag{3}$$

and apparent resistivity

$$\rho_{a,ij}(\vec{r}_l) = \frac{|Z_{ij}(\vec{r}_l)|^2}{\omega \mu_0}, \tag{4}$$

where μ_0 is the magnetic permeability of vacuum.

Conventionally, electric and magnetic fields are recorded at the same location $\vec{r}_l$. The T-MT method (Hermance & Thayer 1975) introduces an inter-site impedance, $\mathbf{Z}_i$, defined as

$$\vec{E}_h(\vec{r}_l) = \mathbf{Z}_i(\vec{r}_l, \vec{r}_b)\, \vec{H}_h(\vec{r}_b), \tag{5}$$

whereby $\mathbf{Z}_i$ is calculated with the E-field measured at the location $\vec{r}_l$ and the H-field measured at the location $\vec{r}_b$ (denoted as base site). Recently, Comeau et al. (2018c) inverted a single profile of MT data across Mongolia and showed that using $\mathbf{Z}_i$ does not compromise resolution and leads to reliable subsurface images. In fact, this approach can further help in suppressing local noise (Egbert 2002; Campanyà et al. 2014).

AS:	Asthenosphere
BF:	Bogd fault
BUF:	Bulnay fault
CV:	Chuluut volcanic zone
EHC:	East Hangai conductor
GAC	Gobi-Altai conductor
GAF:	Gobi-Altai fault
HB:	Hangai block
LAB:	Lithosphere-Asthenosphere boundary
NHC:	North Hangai conductor
SHC:	South Hangai conductor
SHF:	South Hangai fault
TV:	Tariat volcanic zone
TGT:	Tsenkher geothermal area
VL:	Valley of Lakes
VLR:	Valley of Lakes resistor
WHC:	West Hangai conductor

Table 1. Table of abbreviations used throughout the text and in figures.

2.2 Data acquisition

During three field surveys in the years 2016 to 2018, data was collected on a 650×400 km^2 grid (see Fig. 1 and Table 1 for abbreviations of geographic features). The survey covers the Hangai Mountains, a part of the Gobi-Altai mountain range, the Valley of Lakes, and surrounding areas. For the inversion model presented here, we use transfer functions from 272 unique locations with 97 sites laid out on a quasi-uniform grid with 50 km spacing and 175 sites along four profiles (P2, P3, P4, and P6 in Fig. 1) with a spacing of 5 to 15 km. Additional sites are located in the Tariat volcanic field (TV, Comeau et al. 2018a) and the Tsenkher geothermal area (TGT).

We employed two types of instruments: broadband (B) and telluric-only (T). Generally, B-instruments were used for the grid sites, while T-instruments were installed on the profiles. For some of the sites we had to deviate from this scheme due to data quality issues

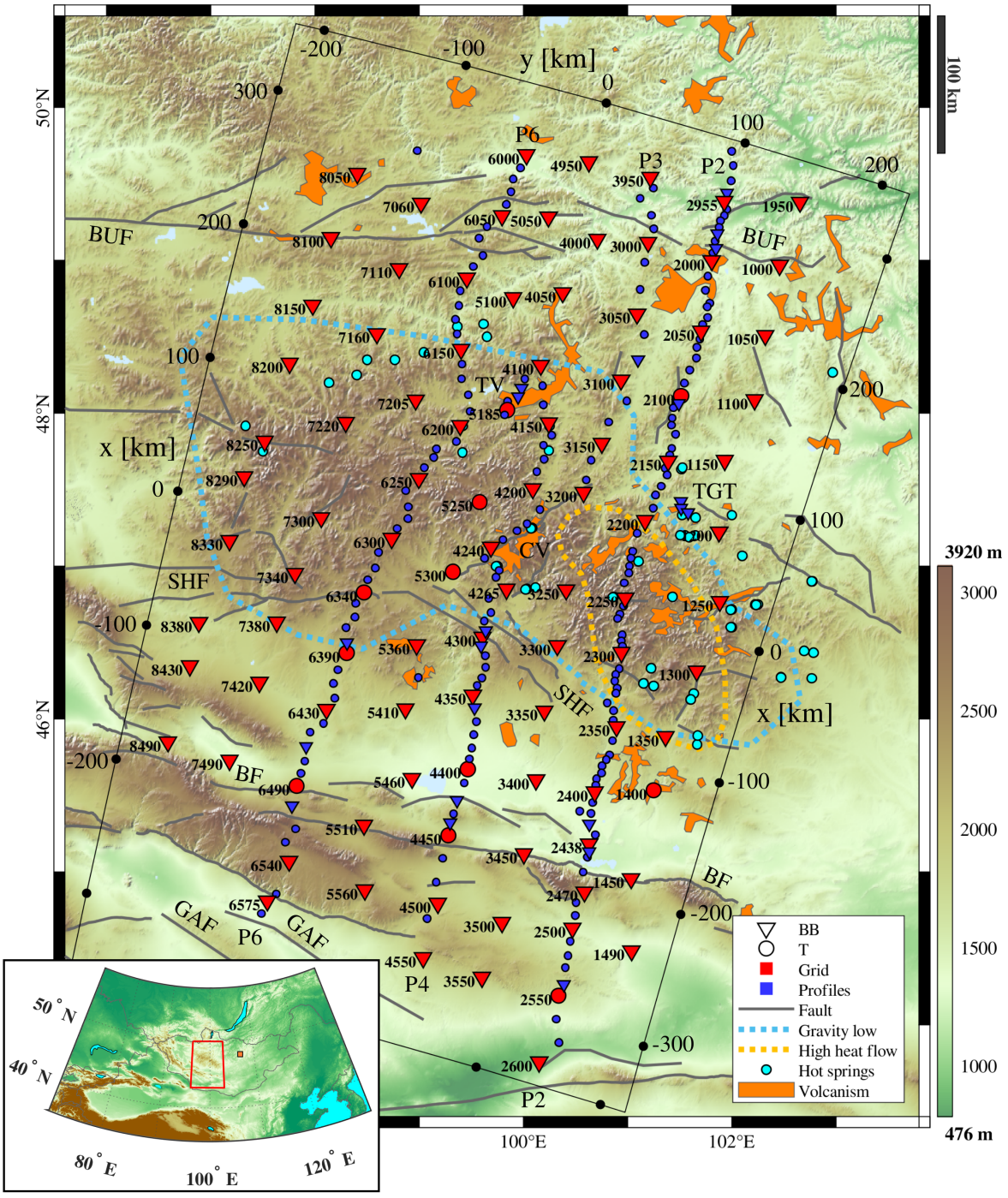

Figure 1. Topographic map with installed sites in central Mongolia. The location in central Asia is indicated in the smaller inset in the lower left. See Table 1 for abbreviations. The symbol indicates the type of instrument used. Red color indicates the grid sites and blue color the others. The grid sites are indicated with their numeric designation. Grey lines mark major fault systems (Walker et al. 2008; Styron 2018), the dotted blue line indicates the -250 mGal Bouguer anomaly (Tiberi et al. 2008), the dotted orange line indicates the 90 mW/m^2 high heat flow anomaly, light blue circles mark hot spring locations (Oyuntsetseg et al. 2015; Ganbat & Demberel 2010), and the orange patches designate Cenozoic volcanic provinces (Ancuta et al. 2018). The black frame around the survey area indicates the rotated local cartesian coordinate system used for the 3-D inversion.

and instrument availability during the measurement campaign. All instruments recorded the horizontal electric field (60 m dipole length with either silver-chloride or lead-chloride electrodes). B-sites additionally recorded all three components of the magnetic field. At B-locations, Metronix ADU-07e and SPAM Mk4 data loggers with Metronix induction coils (MFS-06, MFS-10, MFS-11) were used. Recording was done for three to five days with a sampling frequency of 512 Hz. Additional long period instruments (Geomag Fluxgate and EarthData data loggers) were installed at 14 locations along profiles P2 and P4. Recording time was between 10 and 32 days with a sampling frequency of 2 Hz. The telluric instruments were designed by the University of Münster for fast and easy deployment, thus allowing for efficient data collection with dense site spacing. They recorded with a sampling frequency of 512 Hz for a duration of twelve hours to three days.

2.3 Transfer functions

Impedance tensors were estimated with a robust processing scheme, using the M-estimator (Egbert & Booker 1986) and a minimal covariance determinant method (Rousseeuw 1984; Platz & Weckmann 2019) to improve long period TF when only a few time windows are available (Harpering 2018). To maximise the quality and period range of TF, processing parameters (such as time window selection, bi-coherence threshold values, single site or remote referencing, base site selection for inter-site impedances) were chosen individually for each site. After processing, we obtained a set of 272 TF of high quality in the period range from 0.0078 s to 3000 s at most sites with periods going up to 8000 s and 24000 s for some broad-band and long-period sites, respectively. Fig. 2 shows a representative set of transfer functions at six locations.

Generally, we see that data north of the South Hangai fault (SHF; see 4150BL, 2240T, and 6120T in Fig. 2) exhibit much less spatial variability compared to the sites south of the SHF (1450B in Fig. 2 as well as 2350BL and 4350BL in Fig. 5), which show a very different behaviour. Overall, the data is affected by galvanic distortions. For instance, three of the four sites shown in Fig. 2 (4150BL, 2240T, and 6120T) exhibit a static shift effect

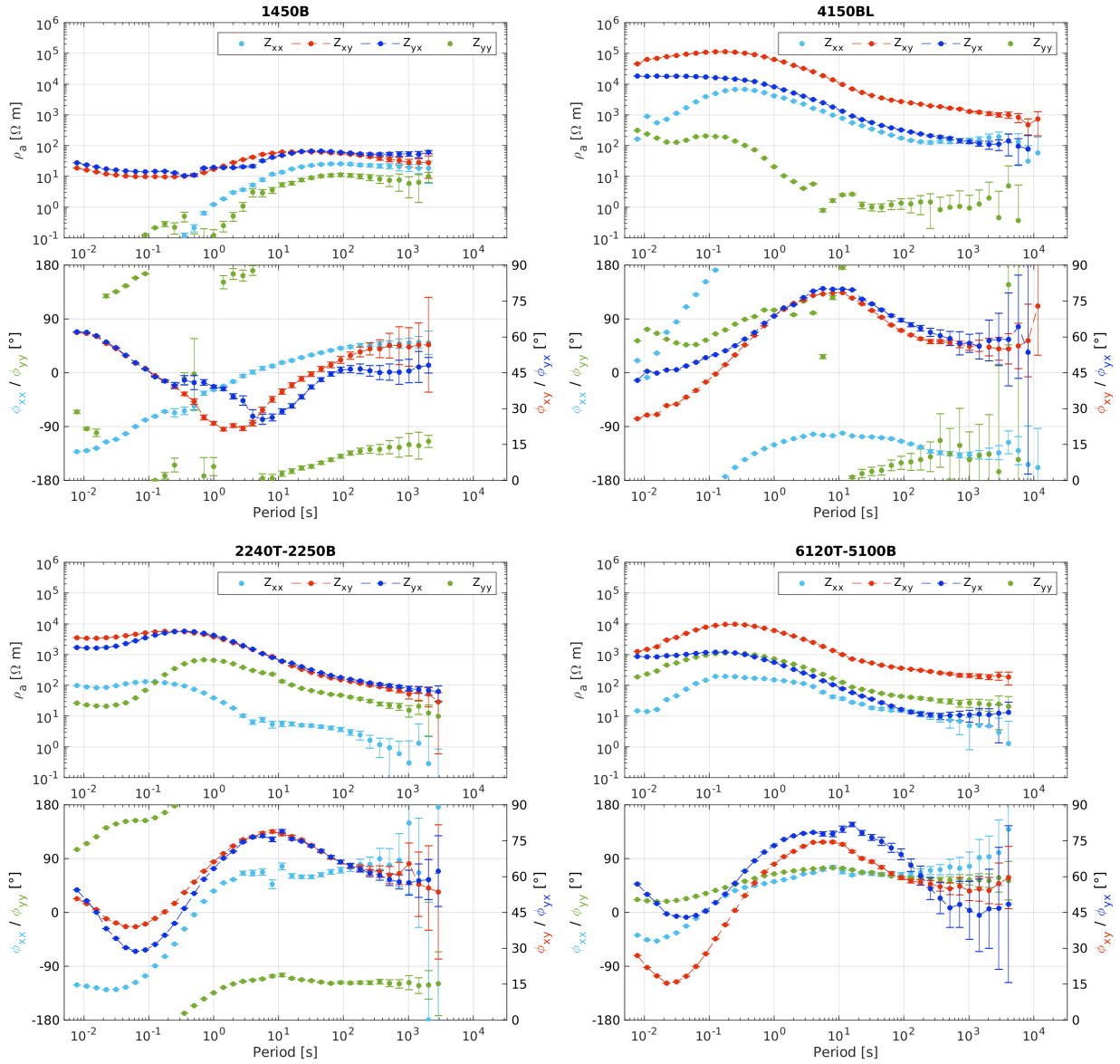

Figure 2. Apparent resistivity and phase curves at six representative sites. The off-diagonal phases (ϕ_{xy} and ϕ_{yx}) are shifted to the first quadrant for better visibility. 1450B is a broadband site, 4150BL is a broadband and long-period site, 2240T and 6120T are telluric sites with their respective base sites given in the plot titles.

(large differences of ρ_{xy} and ρ_{yx} between the sites but with similarly-shaped curves, as well as similar ϕ_{xy} and ϕ_{yx}). Berdichevsky et al. (1980) showed that the static shift effect follows a log-normal distribution and an unbiased regional 1-D impedance can be obtained with the geometric mean of the determinant of **Z**. In this paper, the sum of the squared impedance

elements (SSQ-impedance)

$$Z_{ssq}(\vec{r}_l) = \sqrt{\frac{Z_{xx}(\vec{r}_l)^2 + Z_{xy}(\vec{r}_l)^2 + Z_{yx}(\vec{r}_l)^2 + Z_{yy}(\vec{r}_l)^2}{2}} \tag{6}$$

for each location $\vec{r}_l$ is used to obtain a regional 1-D impedance,

$$\bar{Z}_{\text{1-D}} = \sqrt[N]{\prod_{l=1}^{N} Z_{ssq}(\vec{r}_l)}, \tag{7}$$

where N denotes the total count of locations used. Compared to the impedance determinant, it is less affected by a downward bias due to distortion (Rung-Arunwan et al. 2016). The apparent resistivities and phases obtained from the SSQ-impedances for the grid sites are shown in Fig. 3a for periods $T > 1$ s. Apparent resistivities for northern sites vary over two orders of magnitude, whereas the phase shows smaller variability, especially for periods $T > 10$ s. We conclude that the 1-D impedance calculated from averaged northern SSQ-impedances provides a reasonable representation of the regional 1-D conductivity structure. Southern sites, on the other hand, show a large variability in both ρ_a and ϕ curves over the entire period range, indicating a substantially inhomogeneous regional conductivity distribution. As a result, the southern regional 1-D impedance is likely not representative of a regional conductivity structure.

Further, Fig. 3b shows the real part of the C-response,

$$C = -\frac{\bar{Z}_{\text{1-D}}}{i\omega\mu_0}, \tag{8}$$

calculated for both regional 1-D impedances. It represents the depth of the "center of mass" of induced currents for a given period (Weidelt 1972) and can be used as a proxy for the penetration depth. Starting with a penetration depth of 4-15 km at 1 s, the penetration depth increases to 200 km at the period of 4096 s.

We performed a dimensionality analysis by calculating the phase tensor strike angle θ and the normalized skew angle Ψ (Booker 2014). The polar histograms of θ in Fig. 4 reveal that there are two clear strike directions for periods $T > 10$ s, namely $\approx 15°$ and -75° (clockwise from magnetic North). With a normalized skew angle of $\Psi > 6°$ over a wide period range at the majority of the sites (see the supplementary material, Sec. S1), the collected data

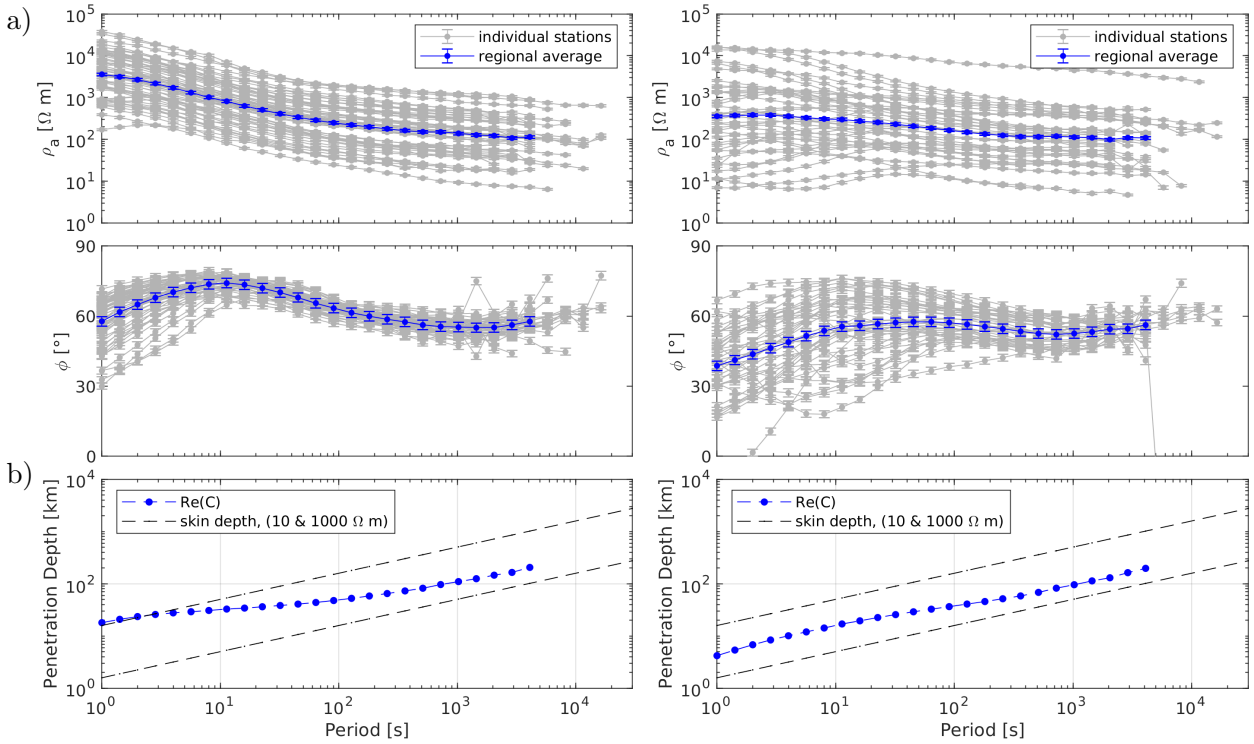

Figure 3. SSQ-impedances and penetration depths estimated from grid site data north (left) and south (right) of the SHF (see Fig. 1). a) ρ_a and ϕ calculated from the SSQ-impedance of each individual site (grey) and from the regional 1-D impedance (Eq. 7; blue). b) The real part of the C-response for both regional 1-D averages, a measure for the penetration depth, together with the skin depths for a homogeneous half space of 10 and 1000 Ωm.

shows a significant influence of 3-D effects (Booker 2014). Thus a 3-D inversion is indeed indispensable to retrieve all information from the dataset.

As was previously shown by Tietze & Ritter (2013), when a predominant geological strike direction exists, it is advantageous to rotate the impedance tensor even for 3-D inversion, thereby improving inversion convergence and reducing modelling errors. Therefore, we rotated the impedance tensors by 15° counter-clockwise, thus aligning the principal axes not only with the strike directions but also the profile directions. An additional benefit of the rotation is the correction of out of quadrant off-diagonal phases, that can be observed at some of the sites. This is shown in Fig. 5 for two sites, 2350BL and 4350BL. For both sites $\rho_{xy} > \rho_{yx}$, indicating East-West oriented low resistivity anomalies. A phase tensor analysis of these sites reveals strong 3-D influences with a normalized skew angle of $\psi > 6°$ in the

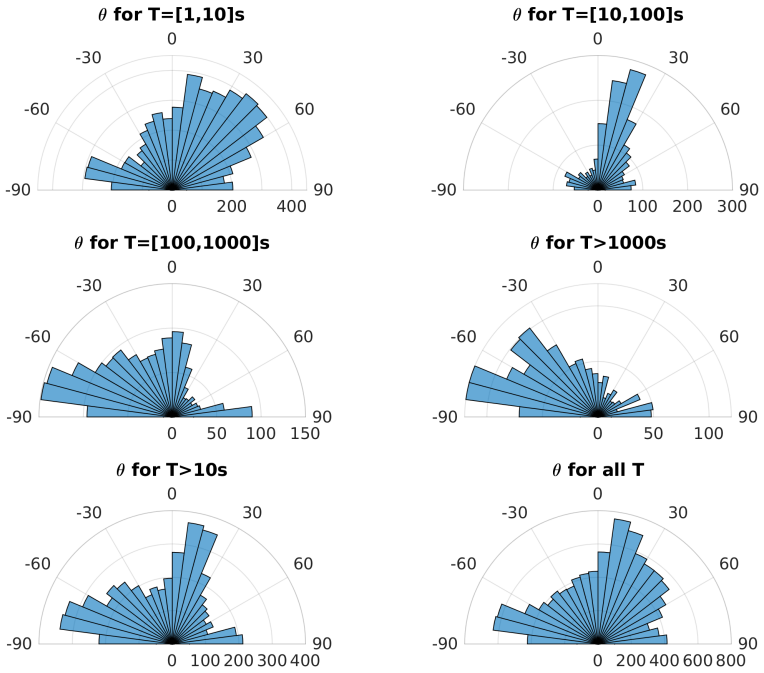

Figure 4. Polar histograms of the phase tensor strike angle θ (clockwise from magnetic North) for different period bands. From 10 s to 100 s a clear strike direction of 15° can be seen, whereas longer periods show a strike of -75°.

period range of 0.1–10 s, indicating that shallow (less than 10 km) 3-D anomalies are most likely the cause of these out of quadrant phases. After rotating the impedance tensor by 15° counter-clockwise from magnetic North, phases remain in their respective quadrants for the entire period range.

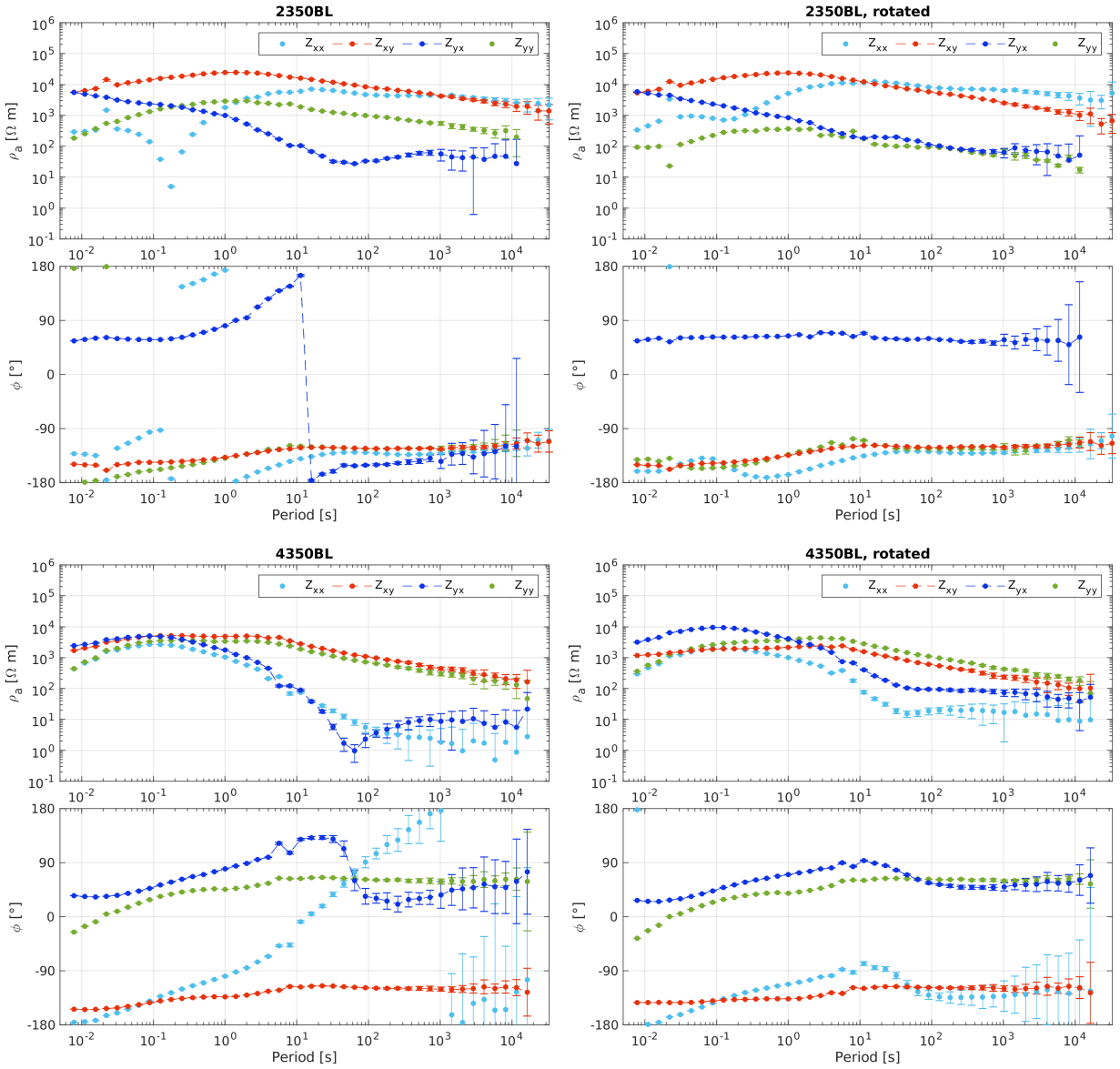

Figure 5. Sounding curves for the sites 4350BL and 2350BL, left: coordinate system oriented along magnetic North, right: rotated coordinate system (15° counterclockwise from magnetic North). After rotation, previously out of quadrant phases remain in their respective quadrants over the entire period range.

3 METHODOLOGY

Owing to the wide frequency range of MT source signals (10^{-4} to $\approx 10^{5}$ s), together with the typical electrical resistivity range of the Earth (0.1 to 10^{5} Ωm), the inversion of MT data can efficiently resolve electrical resistivity variations in a wide range of spatial scales from tens of metres to hundreds of kilometres. MT has been used to successfully image shallow

volcanic and geothermal systems with extents ≈ 10 km with lateral resolution of less than one kilometer (e.g. Heise et al. 2007; Bertrand et al. 2012; Muñoz 2014; Hill et al. 2015; Peacock et al. 2016; Usui et al. 2016; Samrock et al. 2018). At regional scales, MT is commonly used to image crustal and lithospheric structures with a resolution between 1-10 km (e.g. Khoza et al. 2013; Tietze & Ritter 2013; Nieuwenhuis et al. 2014; Cherevatova et al. 2015; Robertson et al. 2017; Xu et al. 2019). In recent years, models obtained by inverting continental scale surveys have appeared with a lateral resolution of tens of kilometres, including the USArray, AusLAMP, and SinoProbe projects (Meqbel et al. 2014; Yang et al. 2015; Robertson et al. 2016; Dong et al. 2016; Murphy & Egbert 2017). However, these surveys rarely bridge multiple spatial scales. The necessary methodological adaptations to the inversion process are outlined below.

3.1 Forward modelling

Electromagnetic fields in a 3-D medium are calculated by solving the following equation

$$\nabla \times (\mu_0^{-1} \nabla \times \vec{E}) + i\omega\sigma\vec{E} = 0 \qquad \text{in} \quad \Omega. \tag{9}$$

Here, $\Omega \subseteq R^3$ is the modelling domain, $\vec{E}$ the electric field vector and σ the electrical conductivity. Further, the inhomogeneous Dirichlet boundary conditions,

$$\vec{E} = \vec{E}_0 \quad \text{on} \quad \partial\Omega, \tag{10}$$

are applied, where $\vec{E}_0$ results from the solution of 2-D Maxwell's equations on the boundaries. The magnetic field $\vec{H}$ is obtained by virtue of Faraday's law. Solutions for two orthogonal source polarisations are computed to be able to derive the full impedance tensor.

The 3-D finite element code GoFEM (Grayver & Kolev 2015) was used to discretize Eq. (9) and find a numerical solution. It is based on the finite-element library deal.II (Alzetta et al. 2018) and uses PETSc (Balay et al. 2018) with METIS (Karypis & Kumar 1999) for distributed linear algebra and mesh partitioning, respectively. The resulting system of linear equations was solved with a parallel version of the iterative FGMRES solver and auxiliary-space multigrid preconditioner as described in detail by Grayver & Kolev (2015). To improve

accuracy of the numerical solutions and to discretize topography accurately, we used locally refined non-conforming hexahedral meshes, as described in Section 3.3.

3.2 Inversion

To obtain the electrical conductivity distribution that explains the measured data we solve a non-linear inverse problem (e.g. Dmitriev et al. 1976; Aster et al. 2018) by minimising the objective function

$$\Phi(\mathbf{m}) = \frac{1}{2}\Phi_d(\mathbf{d}, \mathbf{m}) + \frac{\alpha}{2}\Phi_m(\mathbf{m}), \tag{11}$$

which consists of a data term Φ_d and a model term Φ_m, balanced by the regularization parameter α. $\mathbf{m}$ is a vector of the unknown model parameters (i.e. the electrical conductivity) and $\mathbf{d}$ the data vector, containing the TF. For this study we used the real and imaginary parts of either the regional 1-D impedance (Eq. 7, for a 1-D inversion) or all four impedance tensor components (Eq. 2, for a 3-D inversion). No additional static-shift correction was done.

The data term

$$\Phi_d(\mathbf{m}, \mathbf{d}) = ||(f(\mathbf{m}) - \mathbf{d})||^2_{\mathbf{C}_d^{-1}}\,, \tag{12}$$

contains the difference between the observed and the modelled TFs, which are obtained from the forward modelling operator $f(\mathbf{m})$ given a model $\mathbf{m}$. The data is weighted by the the data covariances $\mathbf{C}_d$, given here by a diagonal matrix containing the data variance δZ^2.

Because of strong galvanic distortions, a relative error e was applied row-wise to the absolute of $\mathbf{Z}$ at each period, giving data variances

$$\delta Z^2_{jx} = \delta Z^2_{jy} = (e \cdot \max(|Z_{jx}|, |Z_{jy}|))^2 \qquad \text{with} \quad j \in \{x, y\}. \tag{13}$$

To prevent imbalance between grid and profile sites, we found that an error $e = 0.03$ for the grid and $e = 0.05$ for the profiles allows us to achieve a uniform fit for all sites. Thereby, TF at the profile sites are slightly down-weighted in comparison to TF from the grid sites.

The model or regularization term

$$\Phi_m(\mathbf{m}) = ||R(\mathbf{m})||^2 \tag{14}$$

is given by the roughness operator $R(\vec{m})$, aimed to stabilize the ill-posed and generally non-unique inverse problem (Tikhonov 1963). No reference model is used in the regularization term. Thereby, the roughness of the model (characterized by the conductivity jumps across the adjacent cells) is minimized.

GoFEM uses the Gauss-Newton method to minimize the functional in Eq. (11) (Grayver 2015). A unit step length for the model update is used. While this can lead to an increase in Φ, it usually allows the inversion to escape a local minimum.

The regularization parameter

$$\alpha = \gamma \frac{||\mathbf{J}^T \mathbf{C}_d^{-1} \mathbf{J}||_2}{||\mathbf{R}||_2} \tag{15}$$

is determined for each iteration step by the ratio of the L_2-norms of the weighted approximate Hessian $\mathbf{J}^T \mathbf{C}_d^{-1} \mathbf{J}$ and the regularization matrix $\mathbf{R}$. $\mathbf{J}$ denotes the Jacobian of $f(\mathbf{m})$. The scaling factor $\gamma \in (0, 1]$ is a user-determined parameter. We adopted a cooling regularization by gradually decreasing the regularization strength through smaller γ. In practice, this approach facilitates the recovery of the dominating large-scale conductivity variations followed by smaller structures later during the inversion process.

3.3 Model discretization

The modelling domain Ω is discretized using hexahedral elements. To ensure numerical accuracy and to decrease the ambiguity of the non-unique problem, we use locally refined meshes. As outlined by Käufl et al. (2018), an initially coarse mesh is locally refined within the area of interest and then transformed to conform to the topography.

The mesh used in this study has a size of $4000 \times 4000 \times 3000$ km^3 and consists of 6800 cells initially. The subsequent refinements were guided by the penetration depth inferred from the C-responses (Fig. 3b). After two refinements at the air-ground interface, three refinements in the central area of interest, and three refinements around site locations, the mesh consists of 215000 cells. Within the survey area, cell diameters range from 4.7 km close to the MT sites to 19 km in the upper mantle down to a depth of 200 km. At greater depths and outside the

survey area, cells increase gradually towards the domain boundary. Finally, the meshes are adjusted to the topography (elevation data provided by NASA JPL 2013) and cells in the air are assigned a resistivity of 10^9 Ωm. The resulting mesh is shown in Fig. 6a. A second finer mesh is obtained by further refinement, resulting in 321000 cells with a minimal cell diameter of 2.4 km near sites (Fig. 6b). This represents our inverse model parametrization.

As is shown by Joshi et al. (2004) and Grayver (2015), it may be advantageous to decouple forward/adjoint and inverse model parametrizations. Specifically, we use an additional refinement step in a 5 km radius around site locations for forward and adjoint solutions in order to better represent local topography and increase numerical accuracy for higher frequencies. A coarser mesh for the targeted parameter (that is, electrical conductivity) reduces computational cost and decrease ambiguity, thereby making the problem less ill-posed. Note that due to hierarchical relation between both forward/adjoint and inverse grids, we avoid any interpolation and simply assign conductivity from the coarser inverse grid cells to refined forward/adjoint grid cells.

Following the arguments from Section 2.3, we perform the inversion in a local Cartesian coordinate system with x- and y-axes rotated 15° clockwise from North and East respectively. The z-axis points downward. The origin corresponds to the center of the survey grid at 47°N, 99.5°E (sea level). All geographic coordinates are transformed into the modelling domain by referencing their UTM coordinates (zone 47, WGS84 reference ellipsoid) to 47°N, 99.5°E followed by a rotation around the origin. The resulting cartesian coordinate system is indicated in Fig. 1.

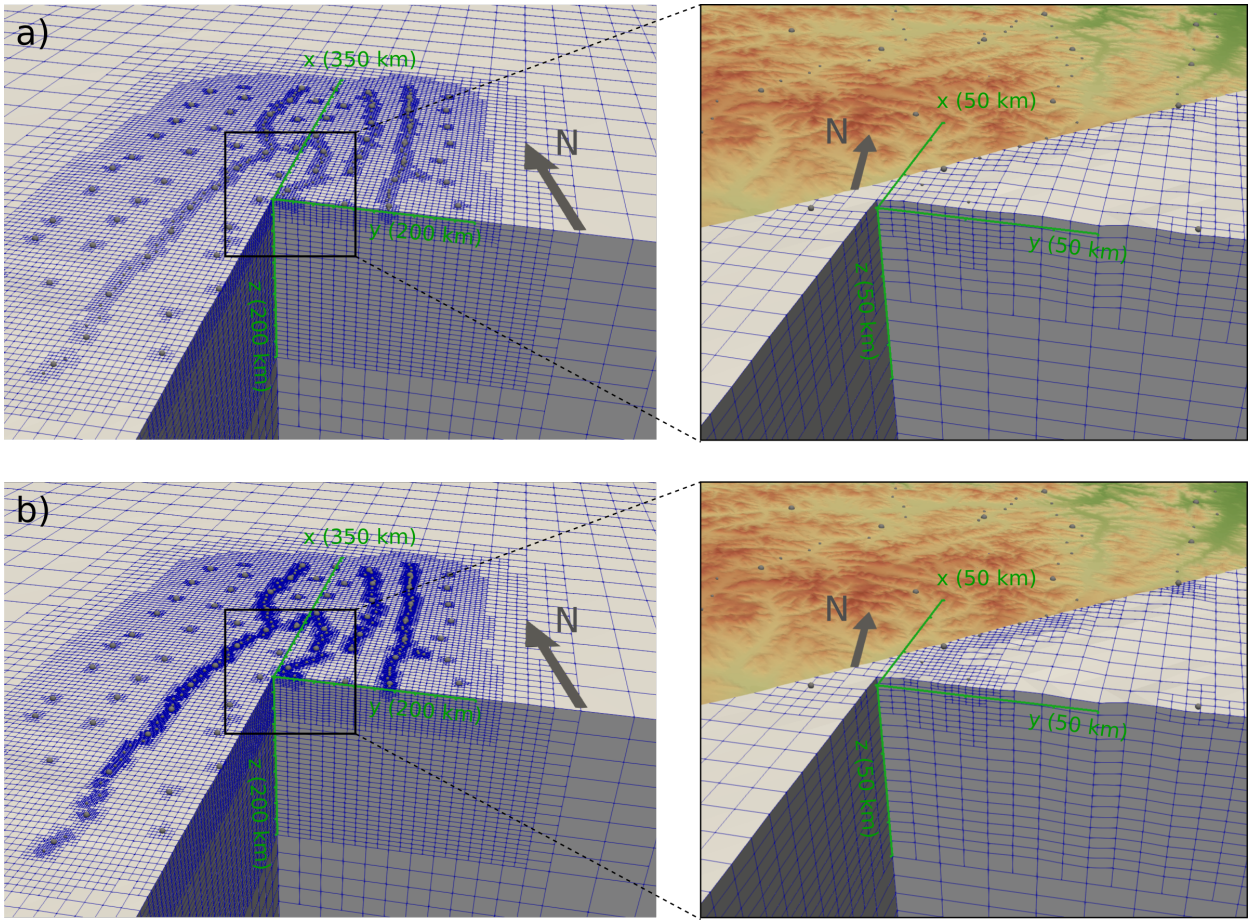

Figure 6. Cutaway view of the coarse (a) and fine (b) inversion meshes as well as a zoomed-in view of the central part. Local Cartesian axes (shown in green) are rotated by 15° clockwise from magnetic North.

3.4 Inversion methodology

We designed a multi-stage approach for inverting the data as shown in the flow-shart Fig. 7. We start by inverting the regionally averaged 1-D impedance $\bar{Z}_{\text{1-D}}$, followed by the 3-D inversion with increasing number of sites and a wider period band. As illustrated in Fig. 7, the final result of each stage is used as the starting model for the subsequent stage, which is done with a finer mesh and more data.

The objective function (eq. 11) has multiple minima. To prevent the inversion from getting trapped in a local minimum that may not correspond to a geologically plausible model, the choice of the starting model is crucial. Rung-Arunwan et al. (2016) proposed to use a 1-D model derived from the regional 1-D impedance (eq. 7) as a starting model.

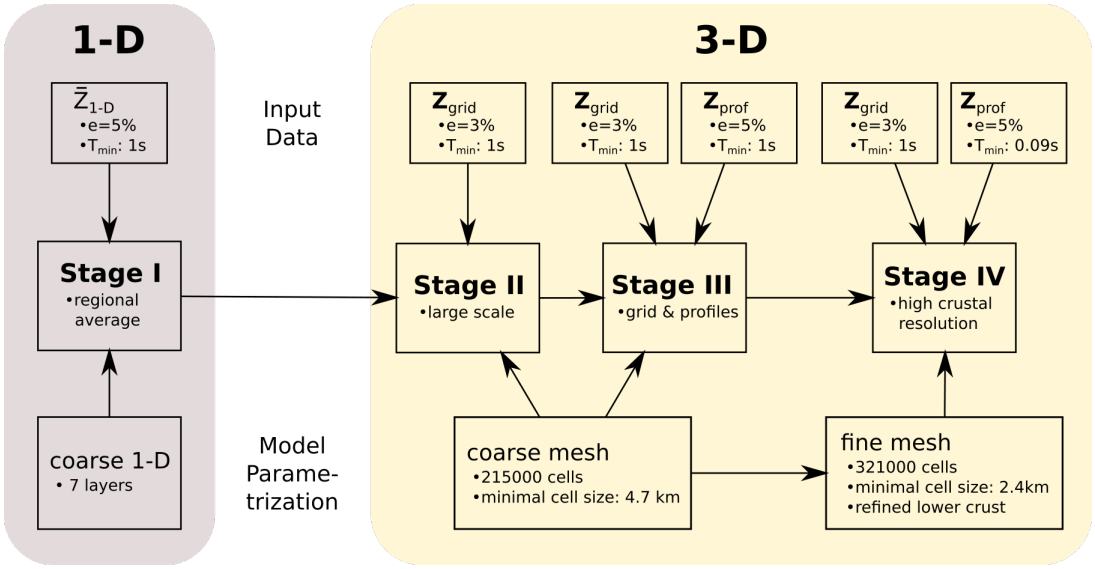

Figure 7. Flow chart of the inversion process, consisting of four stages with different model parametrizations and input data. $\bar{Z}_{1\text{-D}}$ is the regionally averaged 1-D impedance (eq. 7), while $\mathbf{Z}_{grid}$ and $\mathbf{Z}_{prof}$ indicate the 2×2 impedance tensors from grid and profile sites (see Fig. 1). e corresponds to the assigned data error (eq. 13) and the shortest period is denoted by T_{min}.

To calculate the regional average, we used a stochastic inversion algorithm based on the Covariance Matrix Adaption Evolution Strategy (CMAES, see Grayver & Kuvshinov 2016), followed by a Markov chain Monte Carlo (MCMC) walk to evaluate its uncertainty. The obtained 1-D conductivity model is then used as an initial model for the 3-D inversion in Stage II.

For Stage II, only the 2×2 impedance tensors (with $T > 1$ s) from quasi uniformly spaced grid sites $\mathbf{Z}_{grid}$ (red sites in Fig. 1) are inverted. The resulting model is then passed on to Stage III, where 2×2 impedance data from the profile sites $\mathbf{Z}_{prof}$ (blue sites in Fig. 1) are added, most of which are telluric sites with inter-site impedance tensors estimated using the H-field from a nearby full MT station. Based on the result from this step, the final inversion step is performed with the finer mesh (further refinement in the lower crust) and impedances at shorter periods ($T > 0.09$ s). We found that this approach not only reduces computational costs compared to running the inversion on the fine mesh directly, but it also improves convergence significantly and enables the imaging of large and small scale structures within a single model.

4 RESULTS

4.1 Stage I: regional 1-D models

As outlined in Section 3.4, the regional 1-D impedances for sites north and south of the SHF (see Fig. 3) were inverted to obtain 1-D conductivity models (see Fig. 8). The model consists of seven homogeneous layers, consistent with the depth discretization of the 3-D mesh. The best fit models agree with the data well. As outlined in Section 2.3, $\bar{Z}_{\text{1-D}}$ derived from the southern sites is likely not representative of a regional conductivity structure. As a result, we used the 1-D model derived from the northern sites to be the starting model for the subsequent 3-D inversion of the whole region.

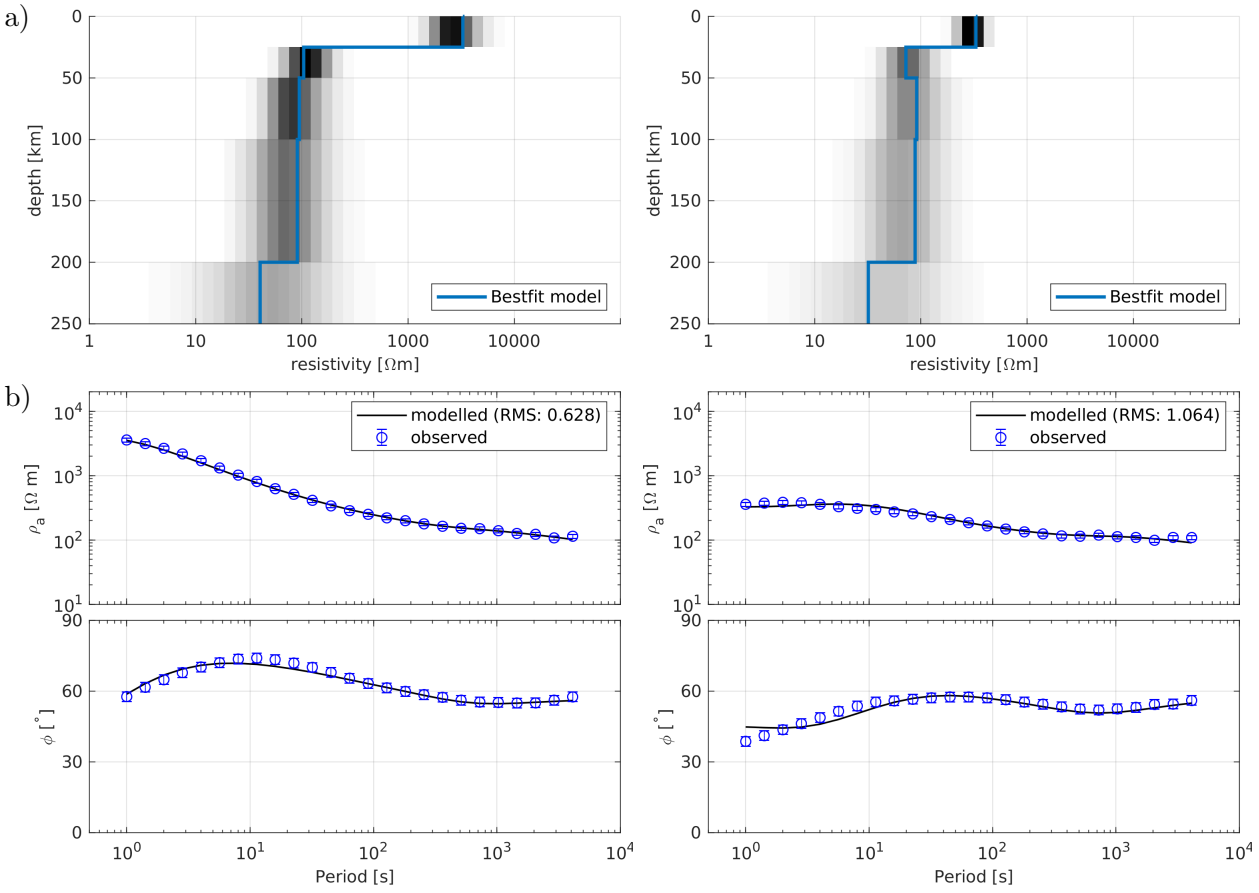

Figure 8. a) Regional 1-D conductivity models (blue), together with a distribution of equivalent models (grey shaded areas) for sites north (left panels) and south (right panels) of the SHF. b) Their data fit for sites north (left panels) and south (right panels) of the SHF.

4.2 Stage II: 3-D large-scale inversion

For this stage, only data from the grid sites (50 km nominal spacing) were inverted. Fig. 9 shows the progressive reduction of the data misfit (as defined by a root-mean squared misfit, RMS) and regularization parameter for each iteration step. As discussed in Section 3.2, the regularization parameter was decreased over the course of the inversion to permit more structure in the model. Starting from an RMS value of 43.1 using the initial 1-D model (see Section 4.1 and Fig. 8), the inversion achieved an RMS value of 2.65 after 19 iterations. Fig. 9a) shows an increase in the misfit for four out of the 19 iterations, indicating an escape from a local minimum or an overshoot, yet this did not prevent the inversion from converging. A continuation with even lower regularization resulted in negligible misfit reductions ($< 3\%$ per iteration) and therefore the inversion was terminated.

The best-fit model (model S2) is shown in Figs 10 and 11 (see Table 1 for abbreviations of geographic and model features). The upper crust is characterised by the resistive Hangai cratonic block (HB) north of the SHF and the very heterogeneous and generally conductive Valley of Lakes (VL) south of the SHF. The Bogd fault (BF) can be traced as a strong conductor. In contrast, the Bulnay and Gobi-Altai Faults (BUF and GAF respectively) are not clearly imaged. At depths of 30 to 35 km below the Hangai, there is an abrupt drop in resistivity of three to four orders of magnitude, most likely indicating a transition to the ductile lower crust . The lower part of the crust (35-50 km) is a heterogeneous conductor, labelled as North, East, South, and West Hangai Conductor (NHC, EHC, SHC, and WHC, respectively). The Valley of Lakes on the other hand is underlain by a resistor (VLR). In the upper mantle (below 50 km) and above the Asthenosphere (AS), resistivities are again higher, except for the SHC and EHC. They extend vertically from the lower crust to the AS.

The single RMS value of the best fitting model is not sufficient to judge its quality (Tietze & Ritter 2013; Miensopust 2017). Instead, the results were evaluated based on the convergence (see Fig. 9), data fit distribution over periods and site locations, as well as histograms of the residuals. Fig. 12 gives a detailed breakdown of the data fit. RMS values

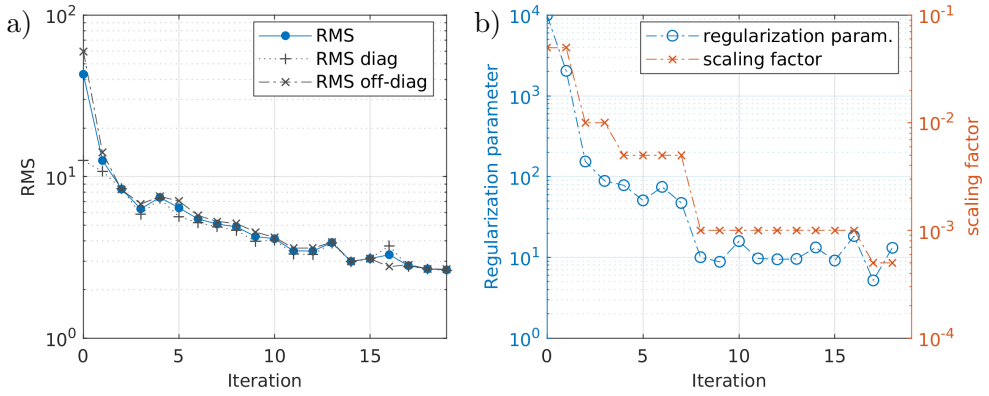

Figure 9. Progression of the RMS value (a) and regularization (see eq. 15) parameters (b) during Stage II of the inversion.

are lowest over the period range from 10 s to 1000 s with slightly higher values for shorter and longer periods, likely because the coarse grid we use still does not allow the introduction of structures to fit the shortest periods, whereas long period data are typically more noisy (due to limited recording times) and difficult to fit. The misfit distribution over individual sites is relatively uniform in the central and northern parts but generally higher in the southern part. The southern part of the model is characterized by strong lateral resistivity variations in the VL and the conductive BF (see the surface panel in Fig. 10). Here, coarse model discretization and regularization prevented the introduction of stronger resistivity variations resulting in poorer fit, which we will improve at later stages. Static shift was largely corrected by the introduction of bow-tie shaped conductivity artefacts (see the surface panel in Fig. 10) close to the sites. Data residuals (see Fig. 12b) exhibit a symmetric and zero-centered distribution, indicating no data-fit pathologies at this stage. The relatively large variance of the distribution will be reduced at later stages.

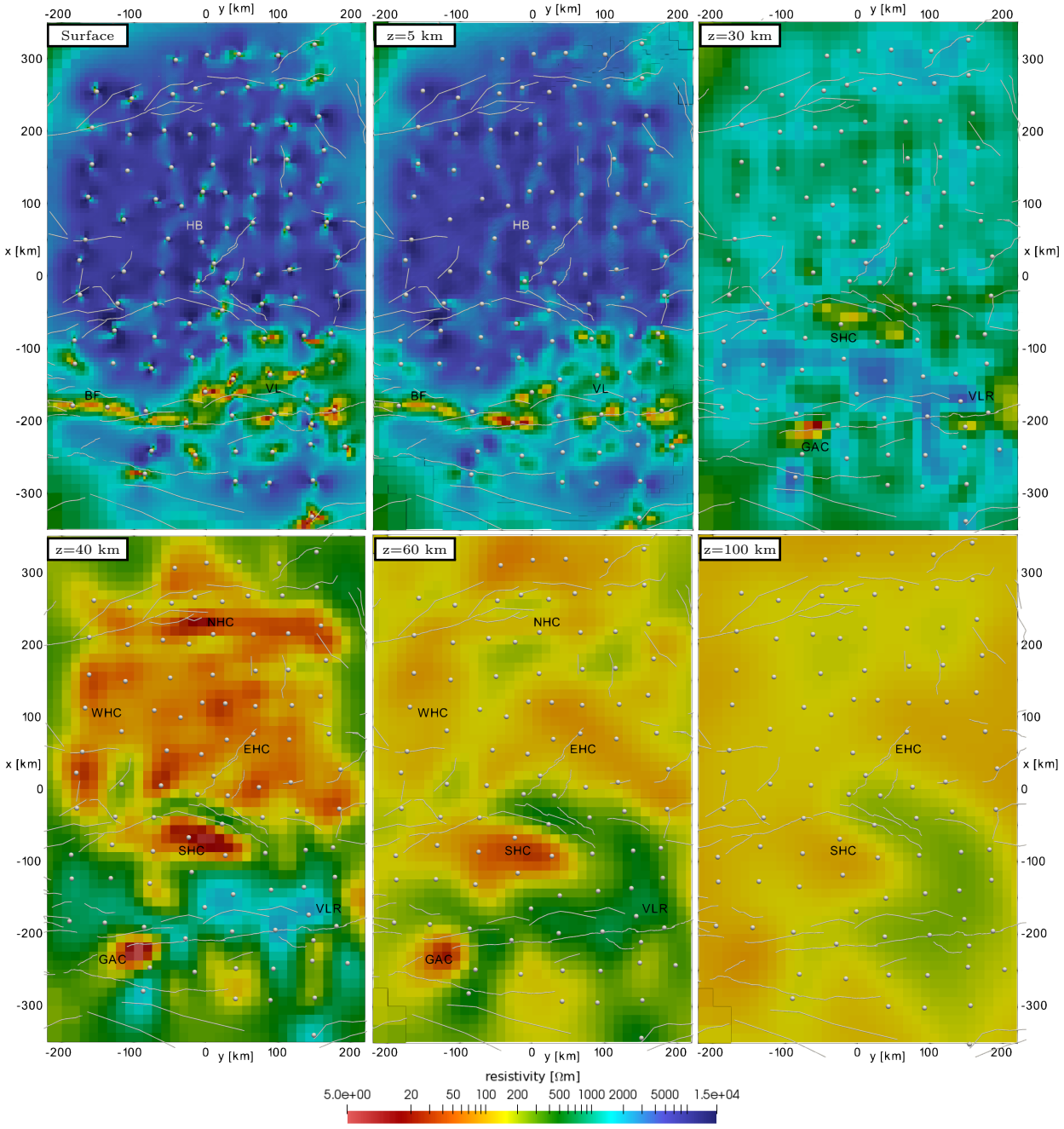

Figure 10. Horizontal slices through the best-fit model of inversion Stage II (model S2). Depth slices are shown at the surface and depths of $z = 5$ km, $z = 30$ km, $z = 40$ km, $z = 60$ km and $z = 100$ km (referred to sea level). Measurement sites are marked with grey spheres and major faults with grey lines. See Table 1 for abbreviations of model features, they include the resistive HB and the heterogeneously conductive VL with the BF in the upper crust. At a depth of 30 to 40 km the resistivity drops abruptly to form five distinct conductors in the lower crust and below, the SHC, NHC, WHC, EHC and GAC. Conversely, the VL is underlain by a resistor (VLR). With greater depths resistivity rises and at 100 km only the SHC and EHC remain discernible.

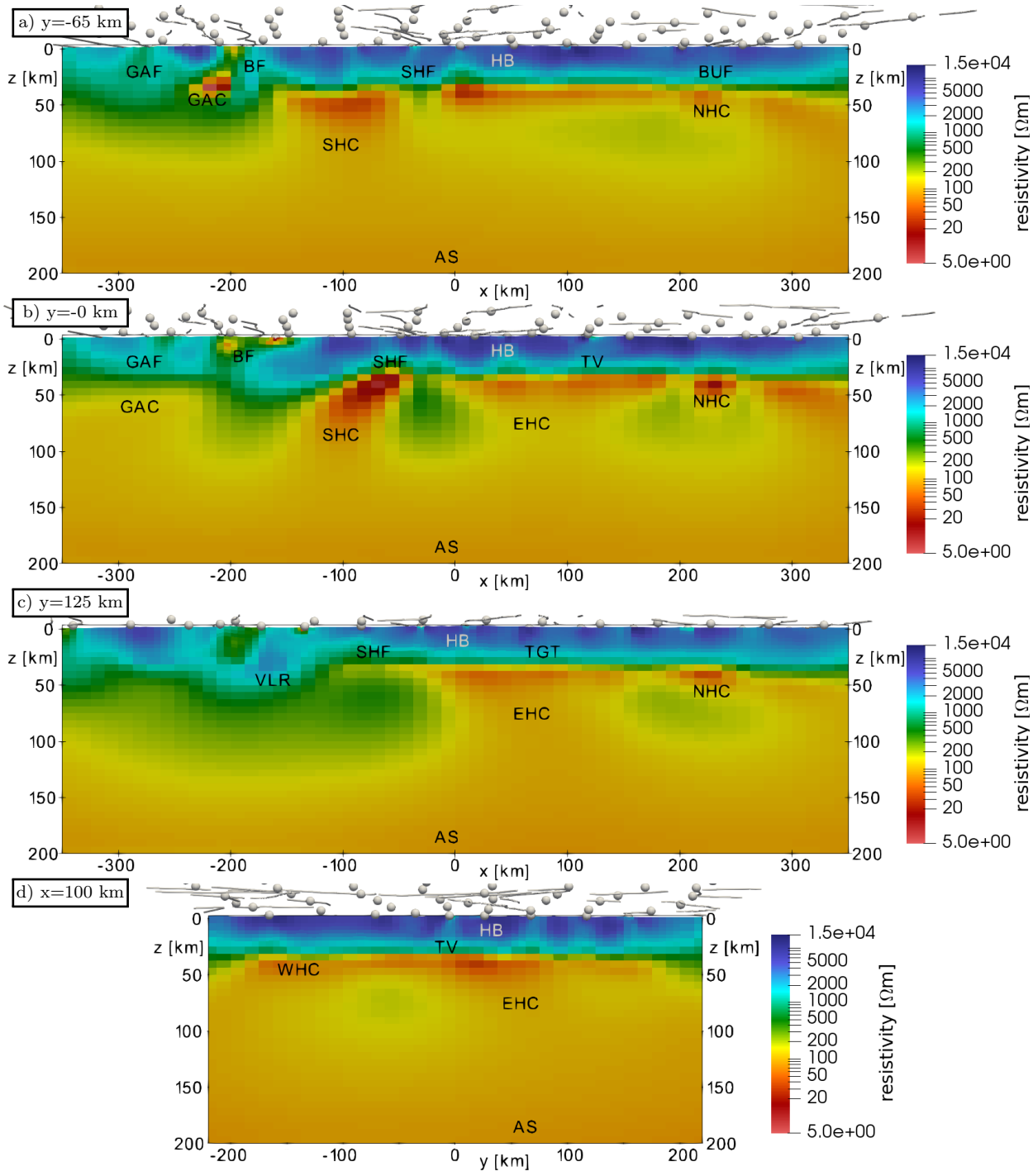

Figure 11. Vertical slices through the best-fit model of inversion Stage II (model S2). The slices are parallel to the x-axis at a) $y = -65$ km, b) $y = 0$ km, c) $y = 125$ km (approximately aligned with profiles 2, 4, and 6, see Fig. 1), and d) parallel to the y-axis at $x = 100$ km. Measurement sites are marked with grey spheres and major faults with grey lines. See Table 1 for abbreviations. The conductive BF can clearly be seen in the upper crust, whereas the GAF and SHF only show up as faint near-surface conductors. Additionally, it can be seen that the NHC is confined to a depth of 40 to 60 km (the lower-most crust), while the EHC and SHC extend downward to the AS. See also Fig. 10 for major model features.

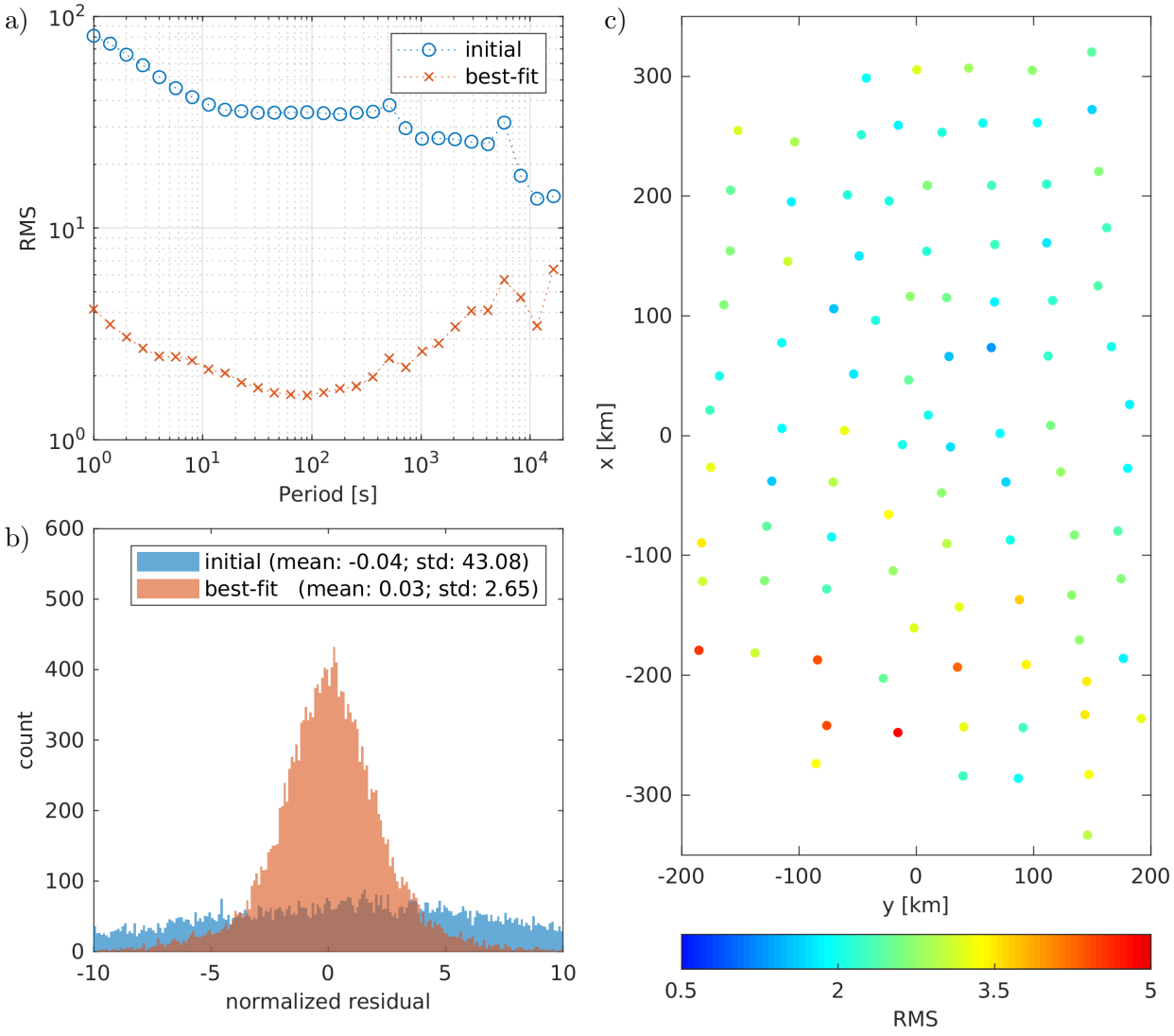

Figure 12. Data fit distribution of inversion Stage II. a) RMS value across periods for the initial and best-fit model; b) data residual histogram for the initial and best-fit model; c) RMS values at measurement sites for the best-fit model.

4.3 Stage III: 3-D inversion of all measurement sites

For the third stage, all measurement sites along profiles and near the TV and TGT were included (mostly telluric-only data). Adding the new data to the previous best fit 3-D model increased the RMS value to 33. After 12 iterations the inversion converged to a model with the RMS value of 2.1. Fig. 13 shows that an RMS value of 3 was reached after only four iterations, owing mostly to the compensated static shift effect. The best fit model (model S3) is shown in Figs. 14 and 15. In comparison to the results from the previous stage (Figs 10

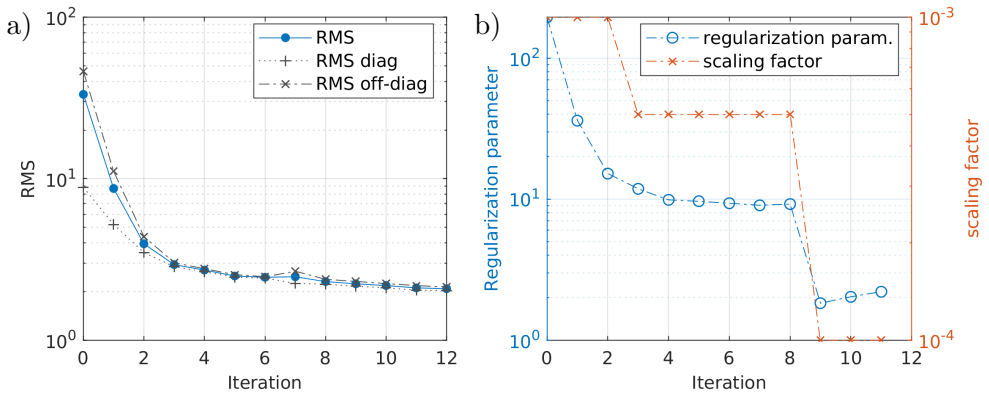

Figure 13. Progression of the RMS value (a) and regularization (see eq. 15) parameters (b) during Stage III of the inversion.

and 11), the large-scale structure remains the same, but resistivity contrasts became better resolved and some crustal structures appear more pronounced, such as the peculiar shape of the NHC. Additionally, the upper crustal resolution is improved (GAF, BF, and SHF) and new structures appear, for example the lowered resistivity in the upper crust below the TV and the TGT.

With an RMS value of 2.1, the data fit (Fig. 16) is overall better than in the previous stage, but with the same characteristics. Specifically, the misfit is slightly higher for short and long periods as well as for the southern sites. Additionally, there are three sites on profile P2 and two sites on profile P4 with a significantly higher misfit. These remaining problems are mainly due to the complex local 3-D structures and are resolved in the final stage of the inversion.

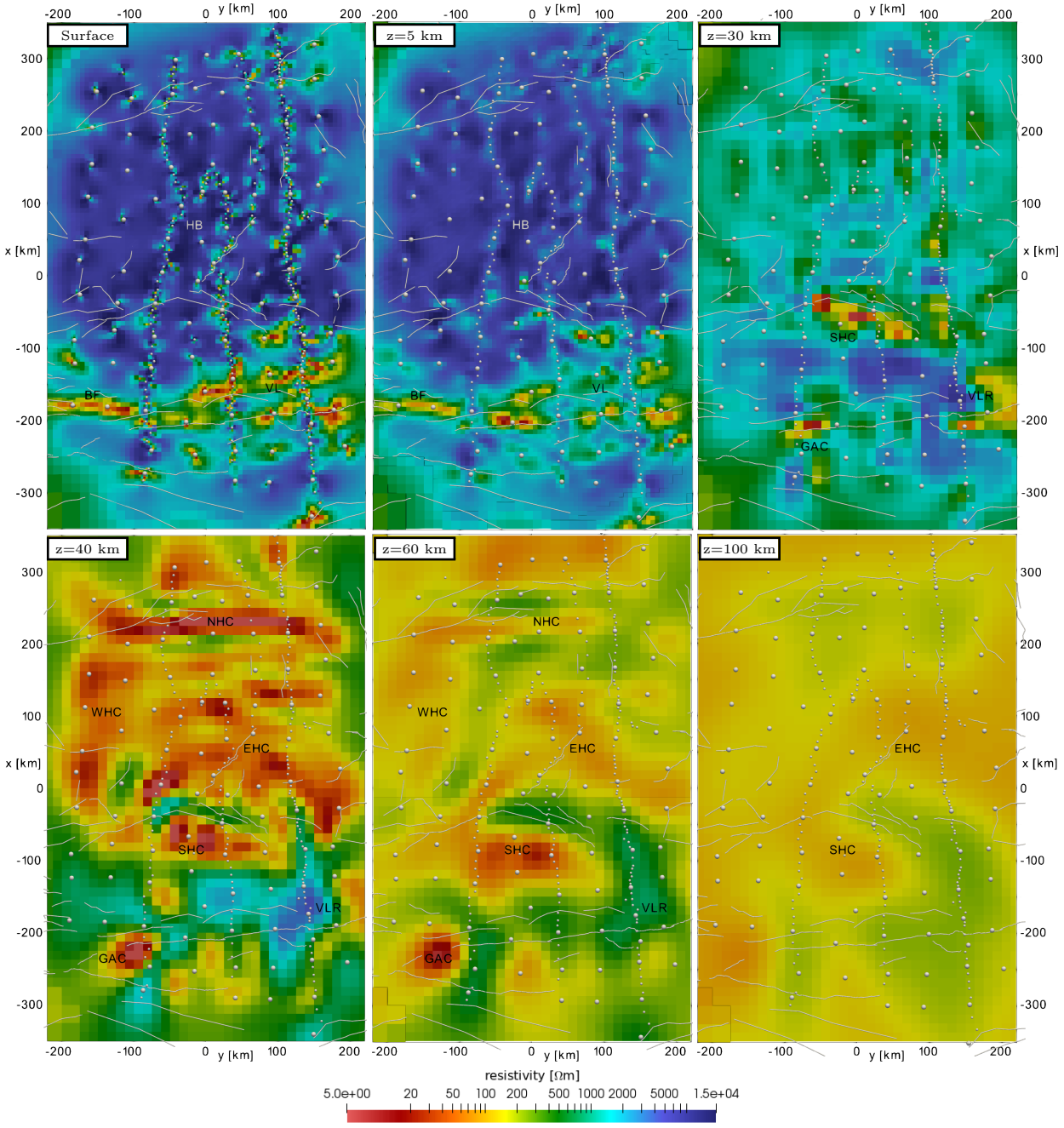

Figure 14. Horizontal slices through the best-fit model of inversion Stage III (model S3). Depth slices are shown at the surface and depths of $z = 5$ km, $z = 30$ km, $z = 40$ km, $z = 60$ km and $z = 100$ km (referred to sea level). Measurement sites are marked with grey spheres and major faults with grey lines. See Table 1 for abbreviations of model features. In comparison to the previous stage (see Fig. 10), model features are imaged more finely. The near surface along the profiles and the conductors in the lower crust ($z = 40$ km) especially benefit from the additional data included in this stage.

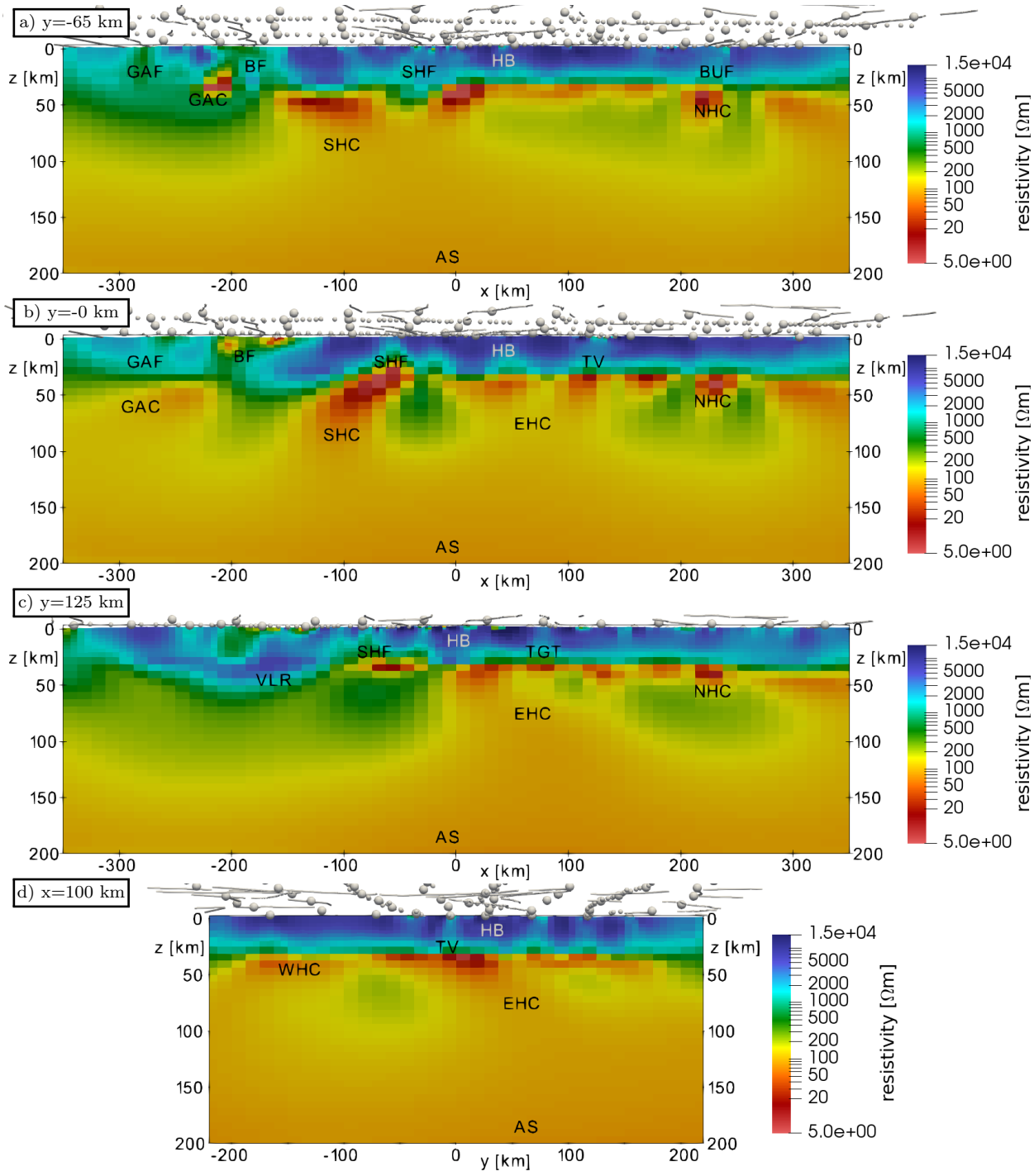

Figure 15. Vertical slices through the best-fit model of inversion Stage III (model S3). The slices are parallel to the x-axis at a) $y = -65$ km, b) $y = 0$ km, c) $y = 125$ km (approximately aligned with profiles 2, 4, and 6, see Fig. 1), and d) parallel to the y-axis at $x = 100$ km. Measurement sites are marked with grey spheres and major faults with grey lines. See Table 1 for abbreviations of model features. See Fig. 10 for major model features. In this model, conductive signatures can be seen in the upper crust below TV and TGT.

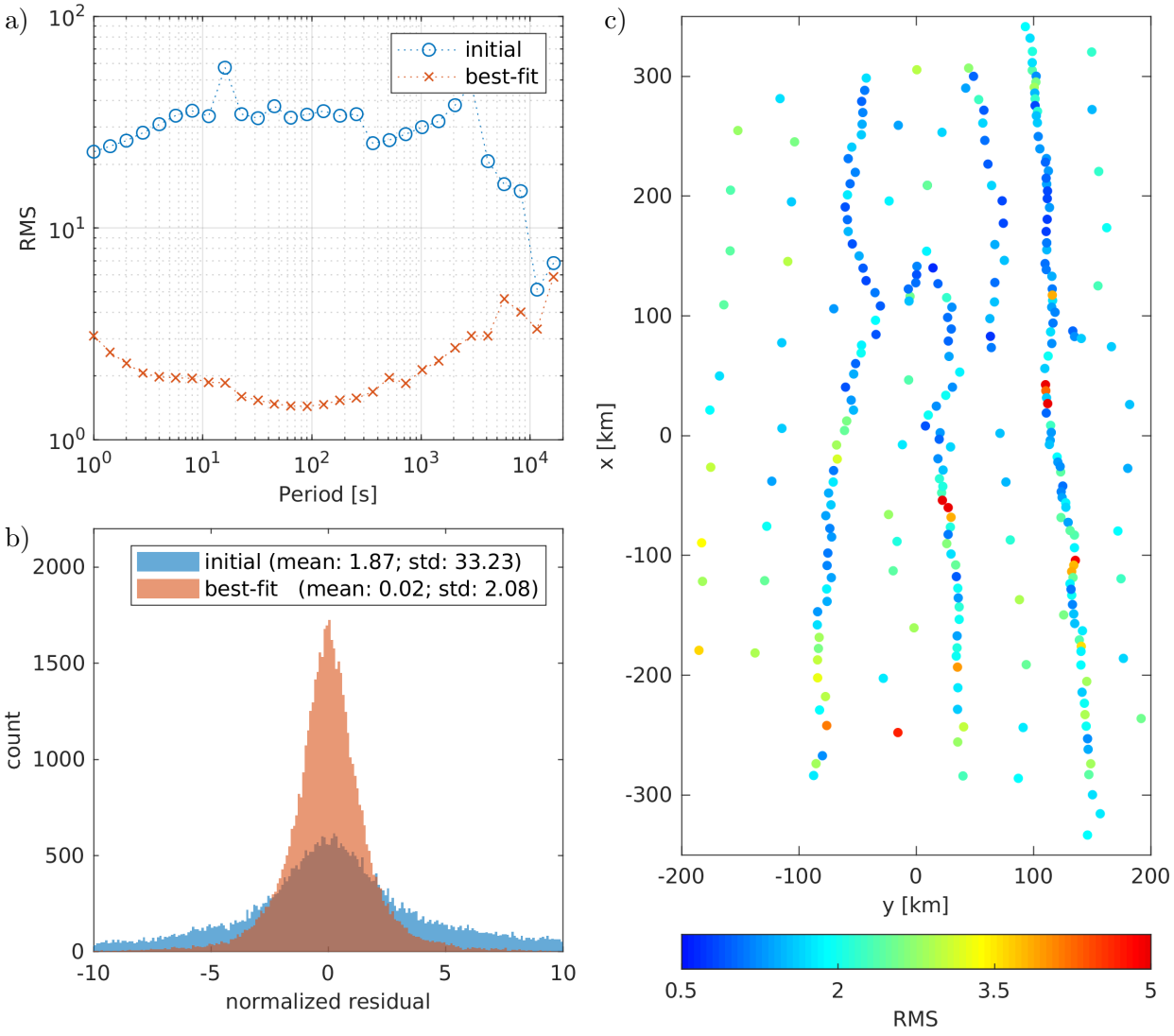

Figure 16. Data fit distribution of inversion Stage III. a) RMS value across periods for the initial and best-fit model; b) data residual histogram for the initial and best-fit model; c) RMS values at measurement sites for the best-fit model.

4.4 Stage IV: higher crustal resolution and short periods

For the last stage, short period data along the denser profiles were added and a finer mesh was used. As we will see, the mesh refinement around site locations and in the lower crust leads to a better fit for short period data.

Adding new data increases the RMS to a value of 8.9 when using the best fitting model from the previous stage. After 17 iterations a misfit of 1.86 was obtained (see Fig. 17). The obtained model (model S4) is shown in Figs 18 and 19. Compared to the previous stage,

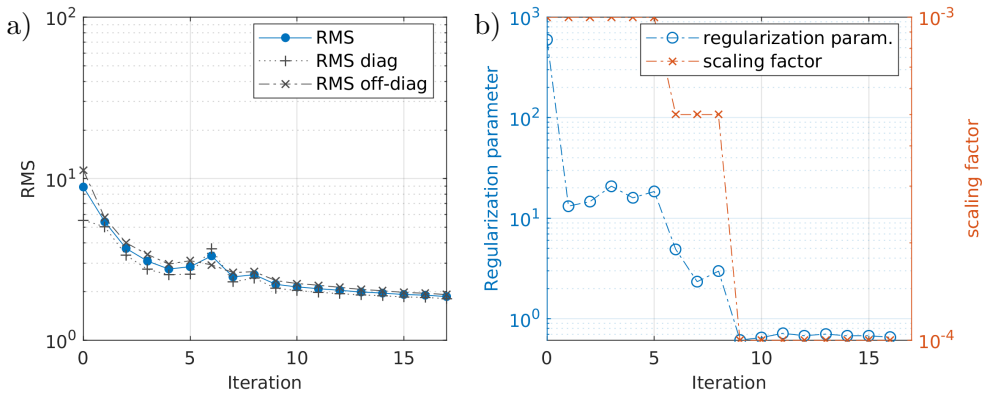

Figure 17. Progression of the RMS value (a) and regularization (see eq. 15) parameters (b) during Stage IV of the inversion.

the finer mesh leads to significantly improved resolution in the lower crust, which further enhanced the geometry and structure of the lower crustal conductors (NHC, EHC, SHC and WHC). By adding the short period data, the crust is imaged more finely and the resolution is close to that of the 2-D model by Comeau et al. (2018c).

The model fits the data well (Fig. 20). The overall higher misfit at longer periods ($>$ 1000 s, Fig. 20a) can be attributed to noisy long period data and the fact that the assigned error was likely too optimistic for these periods. Additionally, there are eight sites that have a RMS values > 3.5, either due to noisy data and poor fit of the diagonal impedance components or because of unresolved local structures.

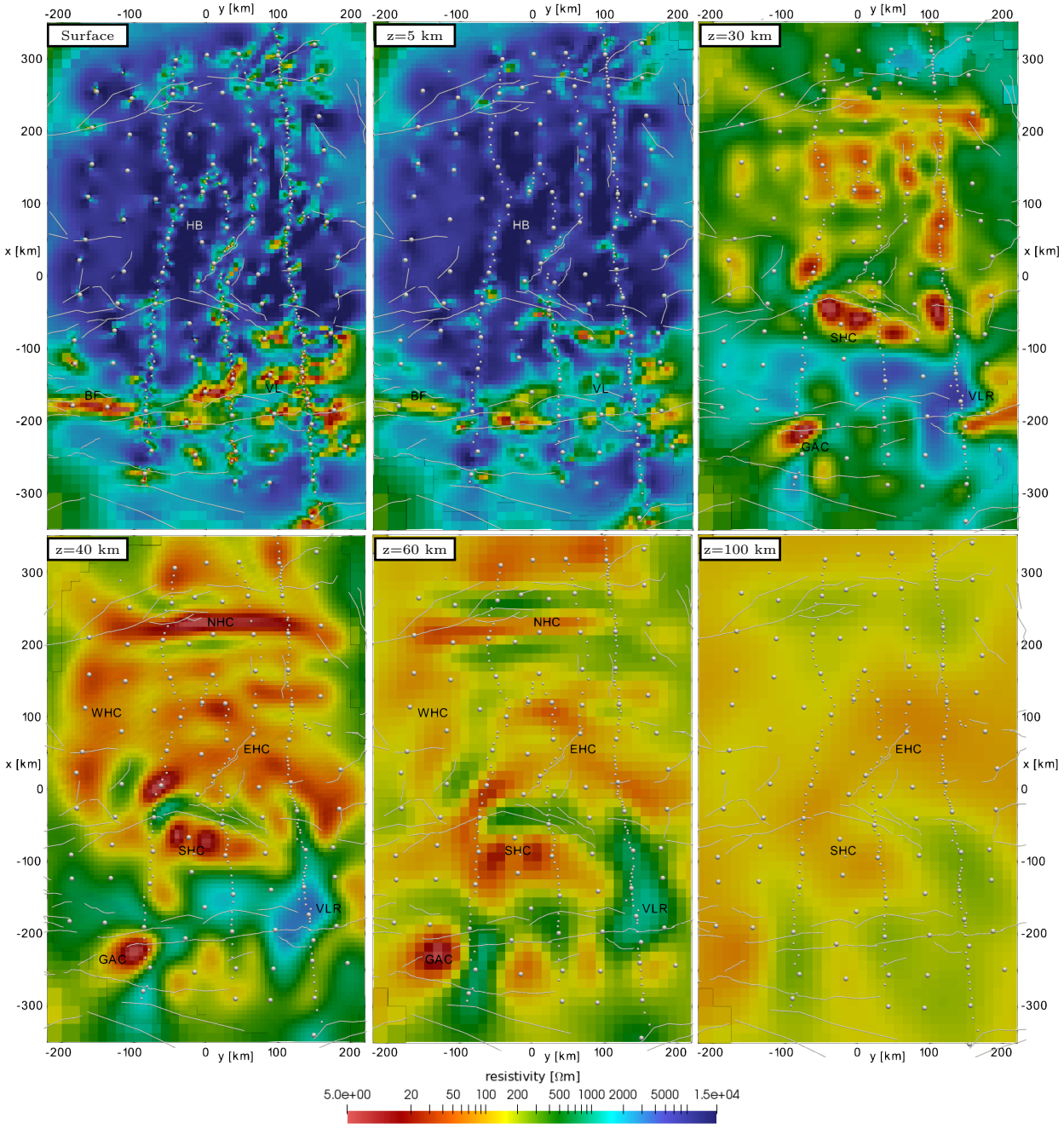

Figure 18. Horizontal slices through the final model of inversion Stage IV (model S4). Depth slices are shown at the surface and depths of $z = 5$ km, $z = 30$ km, $z = 40$ km, $z = 60$ km and $z = 100$ km (referred to sea level). Measurement sites are marked with grey spheres and major faults with grey lines. See Table 1 for abbreviations and Figs 10 and 14 for the model features.

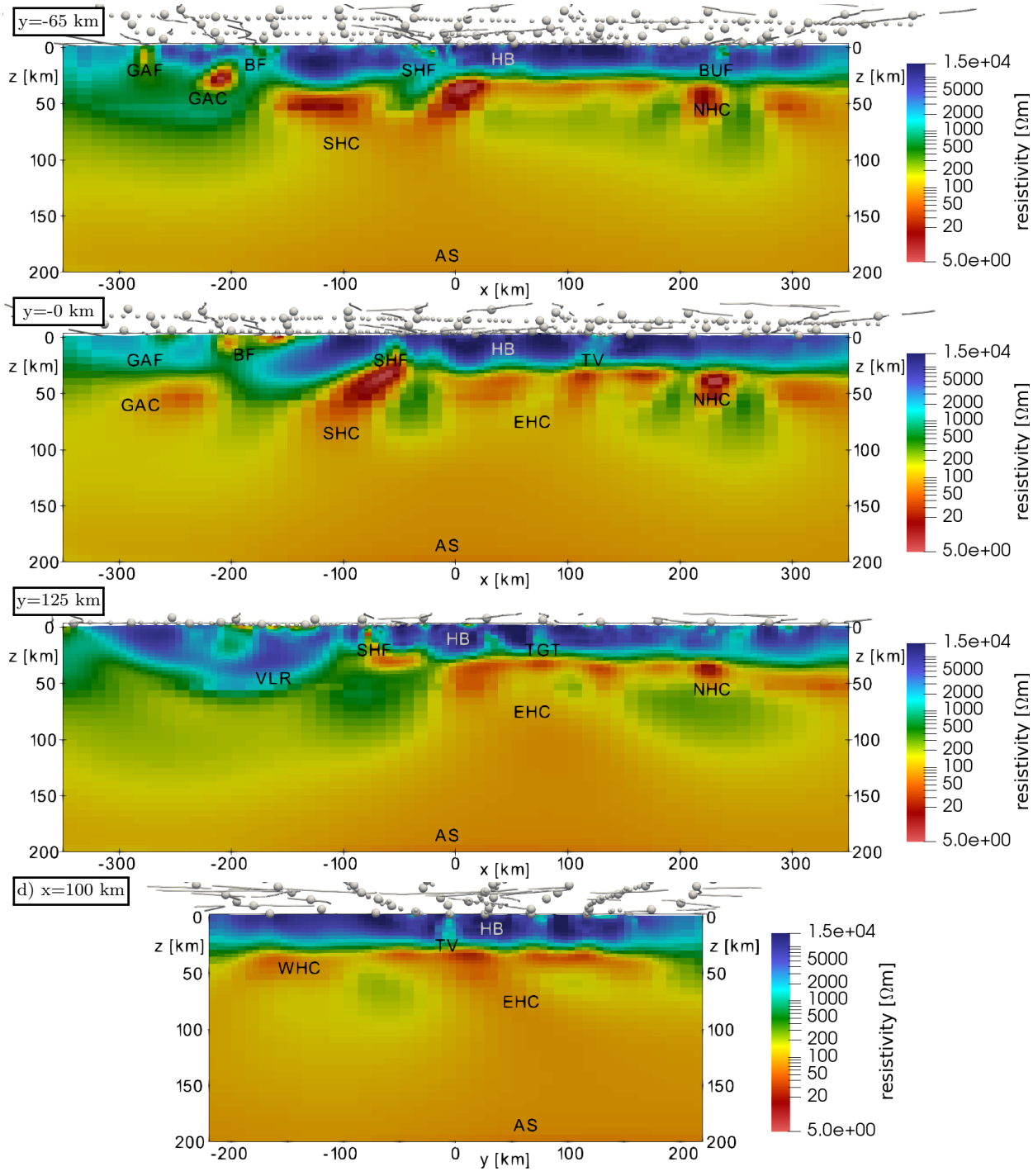

Figure 19. Vertical slices through the final model inversion Stage IV (model S4). The slices are parallel to the x-axis at a) $y = -65$ km, b) $y = 0$ km, c) $y = 125$ km (approximately aligned with profiles 2, 4, and 6, see Fig. 1), and d) parallel to the y-axis at $x = 100$ km. Measurement sites are marked with grey spheres and major faults with grey lines. See Table 1 for abbreviations and Figs 11 and 15 for model features. During this stage the BUF was resolved in some parts of the model.

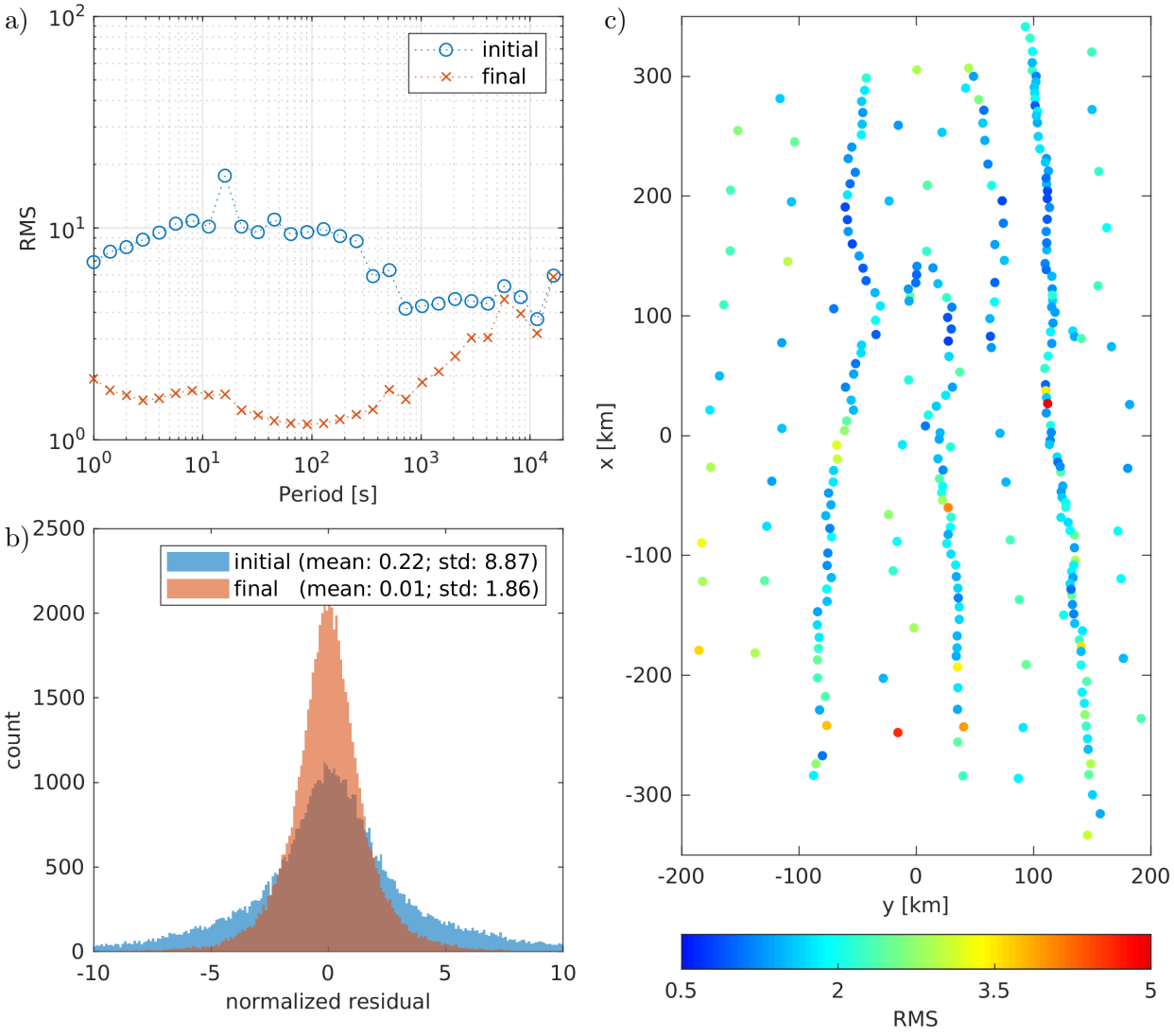

Figure 20. Data fit distribution of inversion Stage IV. a) RMS value across periods for the initial and final model; b) data residual histogram for the initial and final model; c) RMS values at measurement sites for the final model.

5 DISCUSSION

5.1 Inversion methodology

In the previous section, we explained the four stage inversion strategy used to obtain the final resistivity model. Fig. 21 shows a comparison of the models S2, S3, and S4 for an exemplary area in the centre of the model. While larger features (HB, EHC, SHC, etc.) are already imaged in Stage II, the addition of profile sites during Stage III reveals smaller crustal features in more detail (SHF, TV, etc.) and gives a finer resolution for the structure of the EHC in model S3. Additional mesh refinement and the inclusion of short period data improves the results further, as is evident by the comparison of S3 and S4. The link between the SHC and SHF can be seen and TV becomes a prominent vertical conductor in the upper crust, located directly on top of a 40 Ωm conductor at a depth of 35 km. Similar improvements from stage to stage can be observed for other features throughout the model (e.g. TGT, GAF, BUF, BF, CV)

During the first stage, a regionally averaged 1-D model was derived to be used as an initial model for the 3-D inversion. It is well known that the initial model can significantly influence the result of a 3-D inversion. To assess the influence of the 1-D model, we performed two inversion runs with identical settings to Stage II except for initial half-space models of 500 Ωm (Model S2HS500) and 1000 Ωm (Model S2HS1000), see the supplementary material Sec. S3.1 and S3.2. After 18 iterations S2HS500 achieved a RMS value of 3.1 and S2HS1000 achieved a RMS value of 3.2 after 19 iterations. Both are significantly higher than the RMS value of 2.65 achieved after Stage II with a 1-D starting model (Sec. 4.2).

The recovered conductivity structure is similar to S2 only down to a depth of about 70 to 100 km. Below that depth no new features were introduced. Furthermore, it can be seen that the arbitrary choice of the initial half-space resistivity influences the overall resistivity of the final model, the average resistivity of S2HS500 is lower than that of S2HS1000. Although the initial 1-D model from Stage I has an influence on the results of Stage II, there is no arbitrary

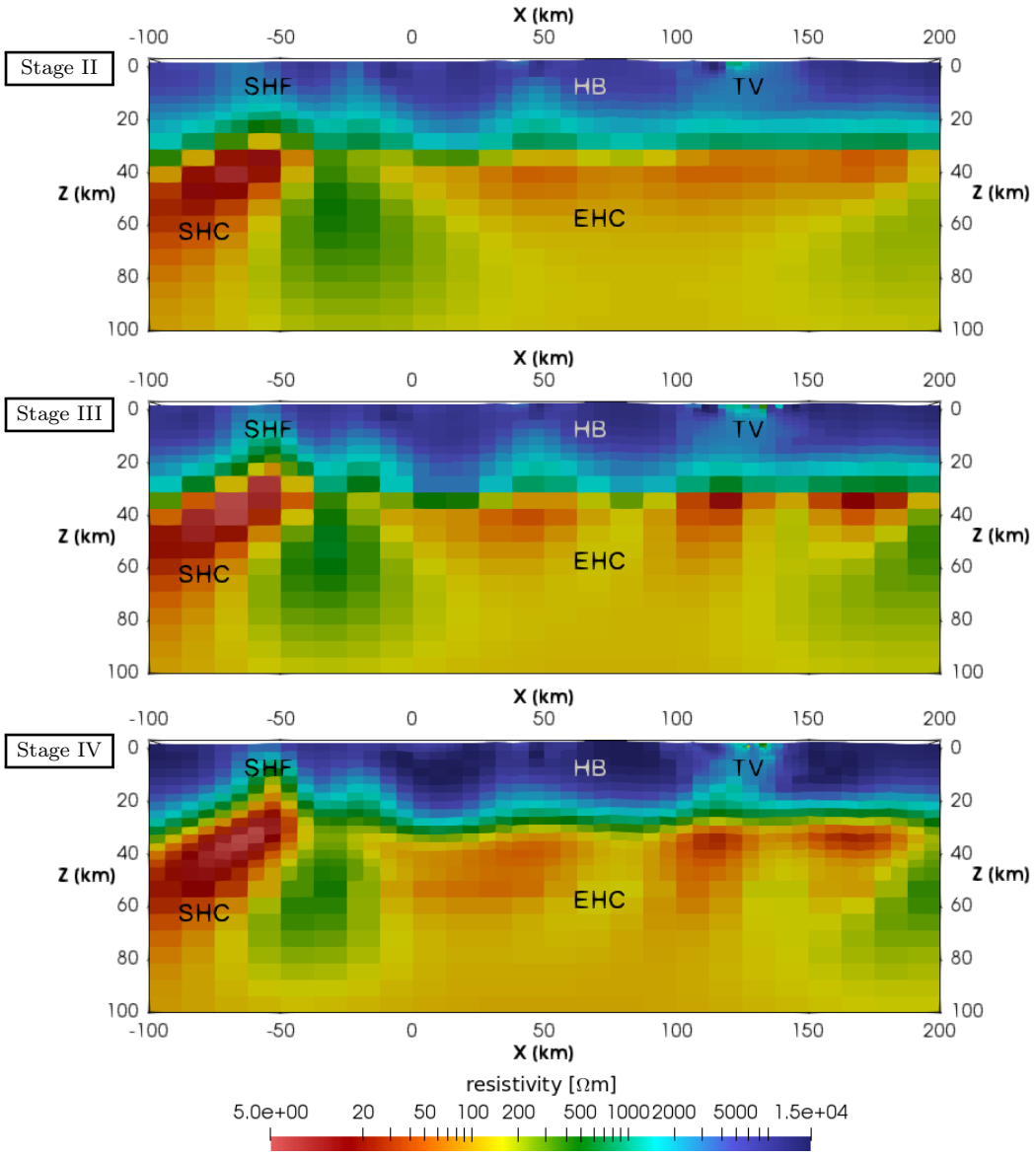

Figure 21. Comparison of the three stages of the 3-D inversion on a vertical slice in x-direction at $y = 0$. See Table 1 for abbreviations and Figs 11, 15, and 19 for major model features.

choice of resistivity values. Instead, the initial model is defined by the regionally averaged impedances and represents the best-fitting 1-D model, with the caveat that measurement sites south of the SHF were discarded (due to the lack of a consistent regional 1-D structure, as outlined in the Sections 4.1 and 2.3). The regional 1-D model north of the SHF is thereby imposed on the region in the south. However, this proves to be not a problem because the 1-D model enters Stage II only as an initial model, not as a reference for the regularization. The strong conductivity contrast at $z = 25$ km (see Fig. 8) is almost completely removed

458 and a laterally more heterogeneous resistivity structure is introduced for the VL and the
459 region south of the SHF to fit the data there.

460 Seperate inversion Stages II and III were necessary to ensure that the regional resistivity
461 structure was recovered first, before smaller and shallow structures were fitted. If the Stages
462 II and III are combined (see Model S2+3 in the supplementary material S3.3) the inversion
463 is strongly biased to the eastern part of the grid (between P2 and P6, see Fig. 1) due to the
464 higher number of stations there. This leads to the western part of S2+3 (west of P6) being
465 fitted only in the end of the inversion process (starting at iteration 15 of 23), resulting in
466 a significantly higher RMS value for sites along line 8, in comparison with the entire grid.
467 The recovered model happens to be virtually identical to model S3. However, because of the
468 bias to the eastern sites for most of the iteration steps, a separated approach is preferred,
469 whereby the regional 3-D structure is recovered from the grid stations first, and afterwards
470 smaller structures are revealed due to the additional data from the profiles introduced during
471 Stage III.

472 For the same reason, short period data (0.09 s to 1 s) with penetration depths as small
473 as 2 km were added in Stage IV, the final stage of the inversion process. The short period
474 data were accompanied by a mesh refinement, which increased the computational cost of
475 a single iteration by a factor of 2.4. By fitting the regional structure on the coarser mesh
476 first and using the fine mesh only in the end, the computational cost for the entire inversion
477 process was significantly reduced.

478

479 5.2 Geologic interpretation

480 *5.2.1 Upper mantle structure*

481 Broad array coverage and the inclusion of long-period measurements enable sensing con-
482 ductivities down to ≈ 200 km. The 3-D model reveals significant low-resistivity ($30-100\ \Omega$m)
483 features (SHC and EHC) below the Hangai Dome at depths greater than approximately
484 70 km, consistent with the previous 2-D model (Comeau et al. 2018c). Calculations confirm

485 that olivine in the upper mantle containing water up to the solubility limit is inadequate
486 to explain the conductivity observed (Yoshino et al. 2009; Comeau et al. 2018c). Therefore,
487 this feature is interpreted as an upwelling asthenosphere that contains partial melt, and it
488 is likely a zone of melt generation. To the south, in the South Gobi region, the LAB depth
489 appears to increases significantly, again consistent with the 2-D model of Comeau et al.
490 (2018c). The geometry of the LAB is consistent with previous seismic profile measurements
491 that indicate an irregular dome-shaped LAB below central Mongolia (Petit et al. 2008).
492 In accord with this interpretation, Bouguer gravity models revealed a localized low-density
493 structure at a depth of $80-125$ km below the central Hangai (Tiberi et al. 2008, see Fig. 1).
494 Furthermore, analysis of erupted mantle xenoliths from central Mongolia suggests long-lived
495 (< 30 Ma) and shallow (< 70 km) melting from an asthenospheric source (Ionov 2002; Barry
496 et al. 2003; Hunt et al. 2012).

497 What is unique about the 3-D model presented here is that, for the first time, the non-
498 uniformness of the asthenospheric upwelling and its lateral complexities are imaged. Two
499 main peculiarities emerge from the recovered shape of the upwelling. Firstly, one arm is
500 imaged below the eastern Hangai Dome, labelled EHC in Fig. 22. It is centred below the
501 eastern part of the dome and dips eastward where it appears rooted at depths greater than
502 150 km. In fact, this anomaly aligns very closely with the location of many cenozoic vol-
503 canic provinces (Ancuta et al. 2018, see Fig. 1), elevated heat-flow measurements (Ionov
504 2002, and references therein, see Fig. 1), indicative of advective heat transfer, and the high-
505 est concentration of present-day hydrothermal activity in the form of meteoric hot springs
506 (Oyuntsetseg et al. 2015; Ganbat & Demberel 2010, see Fig. 1).

507 It is remarkable that these features, together with the upwelling asthenosphere, are con-
508 fined to the estern part of the Hangai Dome. In contrast, there are little known signs of
509 volcanism and geothermal activity in the western part of the Hangai Dome, despite its topo-
510 graphic similarity to the eastern part. Intriguingly, seismic models identified a deep-rooted
511 seismic low-velocity zone further to the east that is reaching upwards below the eastern

512 Hangai and the Hentey plateau (Zhang et al. 2017; Chen et al. 2015) that may represent an
513 extension of the low-resistivity feature observed here.

514 Secondly, a smaller arm of the upwelling asthenosphere is imaged south-west of the
515 Hangai Dome, labelled SHC and depicted in Fig. 23. This is particularly intriguing because
516 it is not below the Hangai Dome itself, but rather south of the dome and the SHF zone.
517 It is, however, below a topographic high. Both arms of the upwelling are connected with a
518 continuous conductive region below 150 km. The origin of such an asthenospheric upwelling
519 remains unexplained. However, it is very likely responsible for the intraplate volcanism
520 observed across the Hangai Dome. In addition it may be responsible for lowering the lower-
521 crustal viscosity by increasing the temperature at the base of the crust.

522 However, it is unknown what relation the smaller secondary arm of the upwelling has to
523 the main arm below the eastern Hangai. Other open questions are whether there exist other
524 arms of the upwelling, for example below the Hovsgol rift region north of the Bulnay fault,
525 and if the volcanism of that region is connected at depth to the same Hangai upwelling.

526

527 ### *5.2.2 Implications for geodynamic models*

528 The origin of the asthenospheric upwelling remains purely speculative at this time. His-
529 torically, explanations for intracontinental uplift have been dominated by arguments for
530 hot, mantle-rooted plumes (e.g. Windley & Allen 1993). However, modern geophysical and
531 petrological evidence is often not consistent with this explanation (e.g. Barry et al. 2003). In
532 central Mongolia, inconsistencies include a lack of low seismic velocities at greater depths,
533 a lack of concentrated high heat flow, low volumes of volcanism, and a lack of spatial or
534 temporal volcanic pattern (e.g. Barry et al. 2003). The moderate resistivity values observed
535 in this study imply low-percent partial melts generated in the mantle due to decompression
536 melting and hence suggest a low-heat flux, small-scale asthenospheric upwelling.

537 From seismic studies, it is known that the lithosphere is thick below the Siberian Cra-
538 ton (up to 225 km), which requires a large lithospheric step (up to 150 km) between the
539 Siberian craton and the Hangai Dome, where the lithosphere is thin (> 70 km). This leads

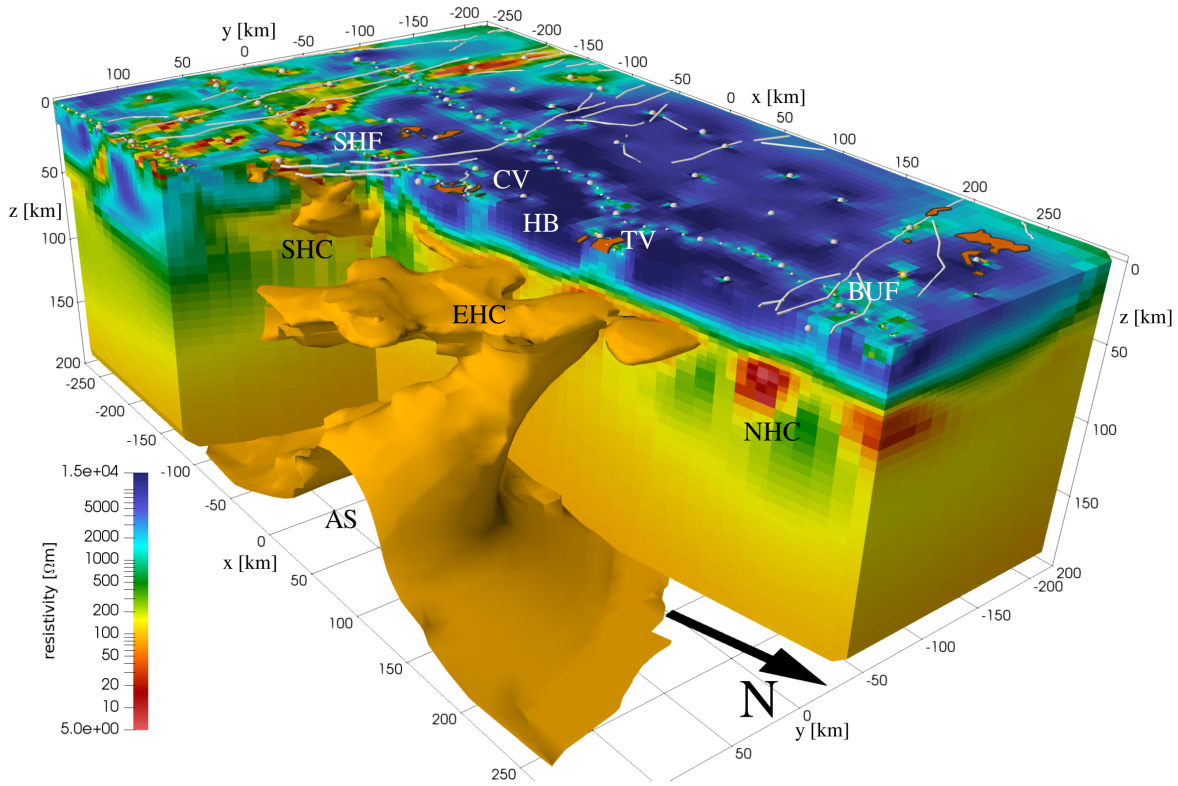

Figure 22. 3-D cutaway view of the model S4. The EHC and the eastern arm of the asthenospheric upwelling are shown with a 85 Ωm isosurface. White spheres indicate measurement sites, white lines are faults, and volcanic provinces are orange.

to speculation that edge-driven convection could cause thermal erosion of the lithosphere (e.g. Bao et al. 2014).

Alternatively, there is good evidence that a delamination event could fit the observational constraints. Previous studies demonstrated that removal or thinning of the sub-crustal lithosphere by a delamination process, whereby the dense sub-crustal lithosphere decouples and peels away from the crust, foundering and sinking into the asthenosphere, results in a small-scale upwelling of the buoyant asthenosphere (e.g. Meissner & Mooney 1998; Kay & Kay 1993; Bird 1979). Critically, numerical modelling studies revealed that a weak lowermost crust, as observed in central Mongolia, is required to trigger a delamination event (Krystopowicz & Currie 2013).

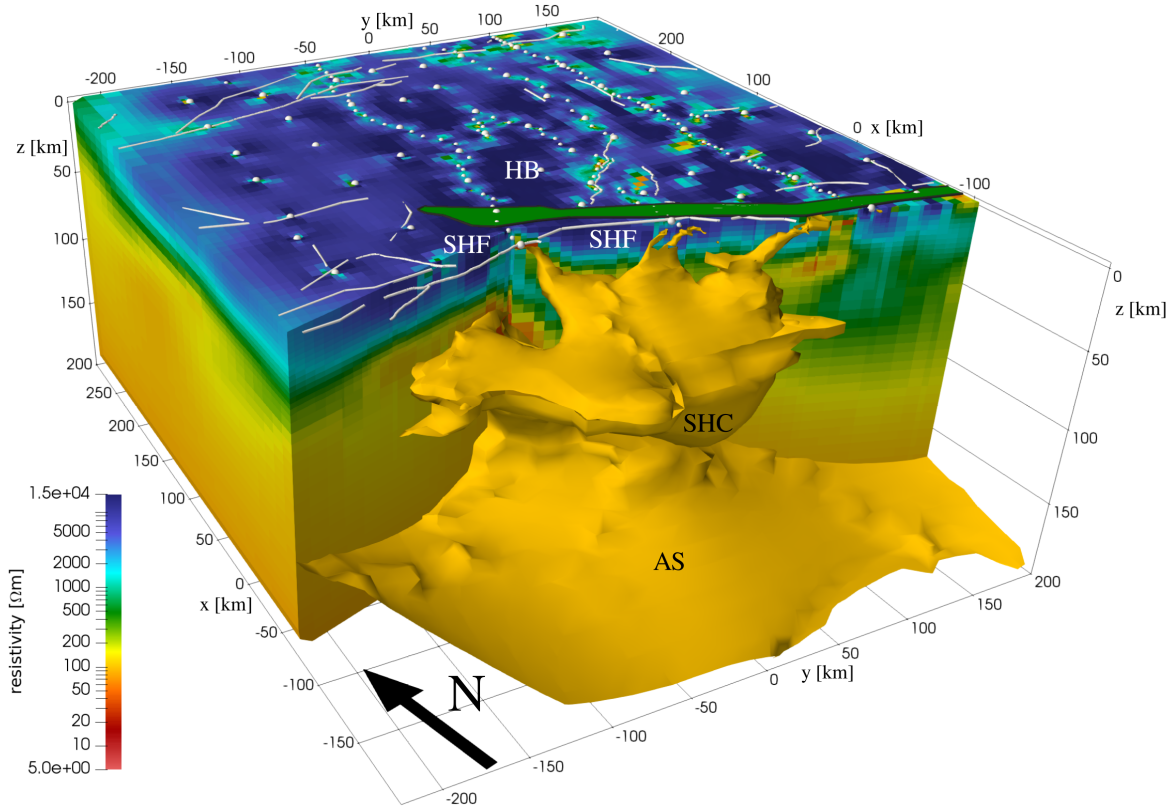

Figure 23. 3-D cutaway view of the model S4. The SHC and the southern arm of the asthenospheric upwelling are shown with a 100 Ωm isosurface. White spheres indicate measurement sites, white lines are faults, and the green area is the Bayankhongor Ophiolite Belt (Buchan et al. 2001).

5.2.3 Lower crustal structure

One of the most prominent and best resolved features revealed by the 3-D resistivity model is the unexpected heterogeneous low-resistivity (10−100 Ωm) zone imaged in the lower crust (30−50 km; labelled EHC, SHC, WHC, NHC). This feature is pervasive throughout the central Hangai but ends abruptly at the South Hangai fault zone. In the northern Hangai region, near the Bulnay fault, this low-resistivity zone is organized into several east-west trending cylinders (with NHC being the most prominent one, see Fig. 18), which is a robust modelling result. The cylinder-like structures have a width of approximately 20 km, and are roughly parallel to the Bolnay fault zone and aligned with GPS measurements that indicate an eastward-motion of the Hangai block (Calais et al. 2003).

Because geochemical evidence is inconsistent with long-lived crustal melt storage below

the Hangai Dome (e.g. Harris et al. 2010), the preferred explanation for these low-resistivity zones are fluids. Highly saline fluids can be exsolved by metasomatism in dehydration and devolatilisation reactions (Manning 2018). Connolly & Podladchikov (2004) predicted that in compressive tectonic settings an inverted stress gradient beneath the brittle-ductile transition causes fluids to become trapped in the lower crust. Furthermore, numerical hydromechanical models can explain how spatial focusing of the fluid source flux can create hydraulically connected fluid-rich domains within the ductile crust (Connolly & Podladchikov 2013). This conceptual model is remarkably consistent with the MT evidence for lower crustal fluid-rich domains in central Mongolia. In addition, the pattern of fluid focusing is expected to be superimposed on large-scale tectonic deformation patterns, such as compression and extrusion. Therefore, in central Mongolia, such fluid-domains should form extended cylinders, compatible with what is observed.

This fluid content substantially changes the rheology and significantly reduces the crustal strength and viscosity (e.g. Liu & Hasterok 2016). This is consistent with evidence from post-seismic slip measurements that also indicate a significantly reduced viscosity in the lower crust of Mongolia, of several orders of magnitude, as compared to the upper crust (Vergnolle et al. 2003). Further evidence for a weak lower crust is given by the depth distribution of local seismicity, no earthquakes are observed deeper than approx. $20-25$ km (Meltzer et al. 2019). A weak lower crust must be considered in future geodynamic and mechanical models of the tectonics in this region. It is an open question how these fluid-rich domains change northwards across the Bolnay fault zone and eastwards outside the Hangai block.

5.2.4 Upper crustal structure

5.2.4.1 Fault zones In general, the upper crust below the Hangai Dome is very resistive ($2000-40000$ Ωm, labelled HB). This can be explained by a pre-Cambrian, cratonic basement (Cunningham 2001). In the VL, the near-surface layer (< 0.5 km) has a highly variable resistivity ($10-2000$ Ωm) caused by porous sediments (Ganbat & Demberel 2010). Elsewhere, some of the anomalous upper crustal features are attributed to fault zones. They

590 are regions of fractured, weakened crust that often have circulating fluids that act to in-
591 crease their conductivity, therefore they are commonly imaged as strong crustal conductors
592 (Unsworth & Bedrosian 2004).

593 South of the Hangai Dome lies the SHF system (Walker et al. 2007; Cunningham 2001),
594 which marks an important terrane boundary (Badarch et al. 2002) and an ancient suture
595 zone created during the closure of the Mongol-Okhotsk ocean (Van der Voo et al. 2015). In
596 the resistivity model the fault zone is imaged as a strong crustal conductor, connected with
597 the SHC and the southern arm of the upwelling (see Fig. 23). However, in contrast to previous
598 2-D results from Comeau et al. (2018c), the conductive feature is not detected continuously
599 along the expected fault trace, instead several disconnected fragments are imaged in the
600 upper crust (Fig. 23). Narrow (< 5 km), tendril like anomalies extend upwards from the
601 SHC in the lower crust to the surface. This may be associated with its mineral potential
602 (discussed below) or that some parts of the fault have been recently reactivated (Walker
603 et al. 2007).

604 Remarkably, the lower crustal conductive zone (discussed above) terminates abruptly
605 at this fault zone. Hence any lower crustal fluids are confined below the Hangai Dome,
606 indicating the importance of this fault zone as a major crustal boundary.

607 Along the northern BUF zone, the resistivity model shows that at near surface depths
608 (< 2 km) conductive anomalies ($50 - 1000$ Ωm) appear coincident with the surface trace
609 of the fault zone in Fig. 22. These can be attributed to a crush zone and to circulating
610 meteoric fluids. However, at depth the fault is not imaged as a strong conductor. Perhaps
611 an electrical signature is absent because the fault is dry and locked, as expected for fault
612 zones with large and infrequent ruptures (Unsworth & Bedrosian 2004; Rizza et al. 2015).
613 Furthermore, it appears the fault zone is independent of the lower crustal fluid zones (no
614 drainage), indicating that the lower reaches of the fault are sealed.

615 The BF zone that runs along the (transpressional) Gobi-Altai mountain range, and which
616 ruptured with a moment magnitude of 8.1 in 1957 (Rizza et al. 2015), is suspected to be
617 lithospheric-scale (Badarch et al. 2002; Calais et al. 2003). Furthermore, this fault zone rep-

618 resents a significant terrane boundary (Badarch et al. 2002). Contrasting crustal properties
619 observed across this zone reflect the rheological differences between accreted terranes of dif-
620 ferent origins (see Guy et al., 2015 and references therein; Comeau et al., 2019). Anomalous
621 conductive features ($30-100$ Ωm) are observed along the GAF system. These dominate the
622 shallow structure and are interpreted to mark terrane boundaries.

623 **5.2.4.2 South Hangai mineralized zones** Immediately south of the SHF is an ob-
624 ducted ophiolite belt, the Bayankhongor Ophiolite Belt (green area in Fig. 23), which is
625 possibly the longest continuous ophiolite belt in the world (Buchan et al. 2001). This region
626 hosts the Bayankhongor Metallogenic Belt, an economically significant ore zone, including
627 important sources of gold and copper.

628 Anomalous, strongly conductive features ($20-40$ Ωm) stretch from the mid-crust to the
629 surface on the the southern edge of the Bayankhongor Ophiolite Belt (see Fig. 23). Miner-
630 alization zones commonly have conductive signatures from associated sulphide mineralogy
631 and metamorphic processes and these are likely imaged in the resistivity model.

632 **5.2.4.3 Tariat and Chuluut volcanic zones** The Hangai Dome contains dispersed,
633 low-volume, intraplate, alkaline basaltic volcanism (average of 50% silica and 4% sodium)
634 (e.g. Ancuta et al. 2018; Hunt et al. 2012; Barry et al. 2003, see Fig. 1 for the volcanic
635 provinces in the Hangai). The Tariat region, the youngest volcanic zone in the Hangai with
636 eruptions as recently as 5000 years ago, contains numerous volcanic cones (approx. 1000 m
637 wide and 100 m high) with volcanic fields from the Holocene (< 11000 years) (Barry et al.
638 2003). The Chuluut region (100 km to the south) is the largest volcanic field in the Hangai.
639 Lavas erupted here, are dated from 6 to 0.3 M years (Ancuta et al. 2018).

640 The MT data are used to generate high-resolution electrical resistivity models in these
641 regions and can give insights into the structure of this region. Anomalous, conductive ($400-$
642 1500 Ωm) features in the upper crust can be seen in Fig. 22 below the volcanic zones of Tariat
643 and Chuluut (TV and CV respectively, along P4). These conductive vertical features in the
644 upper crust may represent hydrothermal alteration from ancient and transient conduits of

hot magma as it moved through the crust by dyking or along pre-existing local crustal weaknesses such as re-activated faults (e.g. Cashman & Sparks 2013), which would produce a small but detectable electrical signature (Comeau 2015; Comeau et al. 2016). No crustal magma storage is expected, due to evidence for fast magma ascent directly from a single parent source at mantle depths from petrological analysis (Harris et al. 2010; Hunt et al. 2012). These anomalous features are spatially associated with the surface expressions of volcanism (volcanic cones and calderas) and modern-day hydrothermal activity (hot springs).

Below these volcanic regions, the upper mantle shows an upwelling asthenosphere (see Sec. 4.4), indicating the source region where melt for the intraplate volcanism is generated (> 80 km). This interpretation supported by petrological analysis of basaltic lavas that indicate long-term partial melting from a single mantle source ($70 - 100$ km). Therefore, the Tariat and Chuluut volcanism can be traced throughout the lithospheric column, from the melt source at the top of the upwelling asthenosphere to the hydrothermal alteration signature of ancient magma conduits in the upper crust. This is, therefore, a nice test of our inversion strategy that was designed to bridge multiple scales.

6 CONCLUSIONS

In this study we present the first 3-D resistivity model of the Hangai and Gobi-Altai region in Mongolia. The presented model successfully resolves features across multiple spatial scales, featuring small (< 5 km) crustal resistivity structures along with large-scale regional resistivity variations (extending more than 100 km) at the Lithosphere-Asthenosphere boundary within the same self-consistent model.

Magnetotelluric data were acquired over an area of 650×400 km^2 in the Hangai and Gobi-Altai mountains in central Mongolia. The project aimed at studying both regional lithospheric setting and the corresponding interactions with shallow crustal features, including local volcanism, geothermal activity and faulting. Therefore, we designed a station layout that combines a regularly spaced 50 km grid with denser spacing along profiles and in local areas of interest that have a spacing as small as 3 to 5 km. Efficient data acquisition

was achieved by the use of telluric-only instruments and deriving telluric-magnetotelluric transfer functions for the profiles.

The technical aspects were addressed by using a finite-element method (FEM) inversion algorithm based on non-conforming hexahedral meshes, which facilitates multi-scale model parametrizations and allowed the incorporation of local topography while keeping computational cost feasible. We further developed a multi-stage inversion methodology, whereby we gradually image various scales by including more sites and using a wider period range. For Stage I, a regional 1-D resistivity model was derived to act as an initial model for the 3-D inversion in Stage II, which included data from the grid sites. The resulting model was then passed on to Stage III, where all sites with denser spacing were added, followed by Stage IV with an extended period range and a finer mesh. This approach decreased the risk of landing in a geologically implausible local minimum of the parameter space. As a result, we obtained a resistivity model that accurately resolves small resistivity structures in the crust together with regional resistivity variations down to the asthenosphere.

This approach can further be extended to both larger and smaller scales. The use of long period instruments on a coarser grid could extend the model resolution beyond the lithosphere-asthenosphere-boundary. A focused inversion, limited to a small subset of the region but using a finer grid and short period transfer functions, could act as a high resolution fifth stage and facilitate local studies of mineralized (Comeau et al. 2018b) and geothermal zones (Batmagnai et al. 2019).

The final model images a prominent low-resistivity zone in the upper mantle, which is attributed to partial melting within an asthenospheric upwelling. It reveals the complex geometry of the upwelling, which appears rooted below the Eastern Hangai Dome with a second smaller upwelling southwest of the Hangai Dome.

Thanks to the resolution across multiple spatial scales, surface observables (such as faults, volcanic provinces and geothermal areas) can be linked with resistivity structures from the shallow upper crust, down to the lithosphere and even asthenosphere. Among them are the locations of the young Tariat and Chuluut volcanic zones, which are associated with

conductive features that can be traced throughout the crust and lithosphere, attributed to past magma ascent and eruption events that have left their electrical signatures due to hydrothermal alteration. Furthermore, the Gobi-Altai and South Hangai fault systems are conductive features that dominate the shallow structures and, in the case of the South Hangai fault system, some surficial conductors are coincident with well known mineralized zones. Interestingly, these conductive anomalies can be traced uninterruptedly downward to the second smaller upwelling southwest of the Hangai Dome.

The crustal structure is dominated by a terrane boundary along the South Hangai Fault System, separating the southern marine terrane of the Gobi Altai from the cratonic Hangai Block. While the upper crust of the Hangai Block is generally found to be highly resistive, the lower crust consists of well-resolved low-resistivity zones in cylinder-like shapes. The strong drop in resistivity at a depth of $30 - 35$ km is interpreted as the transition to the ductile lower crust, in good agreement with the depth distribution of the local seismicity.

The structural information from the resistivity model and their geologic implications will provide crucial information to constrain the formation of the Hangai Mountains and gain insight in intracontinental deformation and intraplate volcanism. The model presented here, is generally consistent with a delamination process as the cause for volcanism and uplift, however, more information is required to validate or disqualify the delamination hypothesis. In this regard, Mongolia is an ideal natural laboratory for studying such intraplate uplift thanks to its location far into the continental interior. It requires crust-mantle interactions to explain observations of intracontinental surface deformation far from tectonic plate boundaries where deformation solely by means of plate tectonics is not possible.

ACKNOWLEDGEMENT

This project was financially supported by the SNF (grant No. 200021L_162660/1) and the DFG (grant No. BE5149/6-1) under the DACH program. This work was supported by the Swiss National Supercomputing Center (CSCS) under project ID s828. We thank the Geophysical Instrument Pool Potsdam (GIPP) and the Geothermal Energy and Geofluids

group (Department of Earth Sciences, ETH Zürich) for providing instruments. We thank the field crew and our colleagues from the Mongolian Academy of Science for their support: Batbileg Tegshjargal, Bayrjarga Bizya, Dominic Harpering, Dorian Sörgel, Eldev-Ochir Bold, Friedemann Samrock, Gantsogt Sukhbaatar, Jörg Schmalzl, Nasan-Ochir Tumen, Neeraj Sudhir, Nomuun Narantsogt, Phillip Kotowski, Robin Mann, Sandra Grazioli, Sukhbaatar Usnikh, Tsagaansukh Halzaa, Tserendug Shoovdor, Zagdsuren Shatar and more. We also want to thank Colin Farquharson and one anonymous reviewer for their detailed comments, which helped improve the manuscript significantly.

REFERENCES

Alzetta, G., Arndt, D., Bangerth, W., Boddu, V., Brands, B., Davydov, D., Gassmöller, R., Heister, T., Heltai, L., Kormann, K., et al., 2018. The deal. II library, version 9.0, *Journal of Numerical Mathematics*, **26**(4), 173–183.

Ancuta, L. D., Zeitler, P. K., Idleman, B. D., & Jordan, B. T., 2018. Whole-rock 40Ar/39Ar geochronology, geochemistry, and stratigraphy of intraplate Cenozoic volcanic rocks, central Mongolia, *Bulletin*, **130**(7-8), 1397–1408.

Aster, R. C., Borchers, B., & Thurber, C. H., 2018. *Parameter estimation and inverse problems*, Elsevier.

Badarch, G., Cunningham, W. D., & Windley, B. F., 2002. A new terrane subdivision for Mongolia: implications for the Phanerozoic crustal growth of Central Asia, *Journal of Asian Earth Sciences*, **21**(1), 87–110.

Balay, S., Abhyankar, S., Adams, M. F., Brown, J., Brune, P., Buschelman, K., Dalcin, L., Dener, A., Eijkhout, V., Gropp, W. D., Kaushik, D., Knepley, M. G., May, D. A., McInnes, L. C., Mills, R. T., Munson, T., Rupp, K., Sanan, P., Smith, B. F., Zampini, S., Zhang, H., & Zhang, H., 2018. PETSc users manual, Tech. Rep. ANL-95/11 - Revision 3.10, Argonne National Laboratory.

Bao, X., Eaton, D. W., & Guest, B., 2014. Plateau uplift in western Canada caused by lithospheric delamination along a craton edge, *Nature Geoscience*, **7**(11), 830.

Barry, T., Saunders, A., Kempton, P., Windley, B., Pringle, M., Dorjnamjaa, D., & Saandar, S., 2003. Petrogenesis of Cenozoic basalts from Mongolia: evidence for the role of asthenospheric versus metasomatized lithospheric mantle sources, *Journal of Petrology*, **44**(1), 55–91.

Batmagnai, E., Samrock, F., Grayver, Alexander, V., Kuvshinov, A., Saar, Martin, O., Demberel, S., Tsegmed, B., Tserendug, S., Purevsuren, D., & Oyuntsetseg, D., 2019. Integrated geoscientific

exploration for geothermal energy utilization in the Mongolian Hangai, in *EGU General Assembly Conference Abstracts*, Vienna, Austria.

Berdichevsky, M., Vanyan, L., Kuznetsov, V., Levadny, V., Mandelbaum, M., Nechaeva, G., Okulessky, B., Shilovsky, P., & Shpak, I., 1980. Geoelectrical model of the Baikal region, *Physics of the Earth and Planetary Interiors*, **22**(1), 1 – 11.

Bertrand, E., Caldwell, T., Hill, G., Wallin, E., Bennie, S., Cozens, N., Onacha, S., Ryan, G., Walter, C., Zaino, A., et al., 2012. Magnetotelluric imaging of upper-crustal convection plumes beneath the Taupo Volcanic Zone, New Zealand, *Geophysical Research Letters*, **39**(2).

Bird, P., 1979. Continental delamination and the Colorado Plateau, *Journal of Geophysical Research: Solid Earth*, **84**(B13), 7561–7571.

Booker, J. R., 2014. The magnetotelluric phase tensor: A critical review, *Surveys in Geophysics*, **35**(1), 7–40.

Buchan, C., Cunningham, D., Windley, B. F., & Tomurhuu, D., 2001. Structural and lithological characteristics of the Bayankhongor Ophiolite Zone, Central Mongolia, *Journal of the Geological Society*, **158**(3), 445–460.

Cagniard, L., 1953. Basic theory of the magneto-telluric method of geophysical prospecting, *Geophysics*, **18**(3), 605–635.

Calais, E., Vergnolle, M., San'Kov, V., Lukhnev, A., Miroshnitchenko, A., Amarjargal, S., & Déverchère, J., 2003. GPS measurements of crustal deformation in the Baikal-Mongolia area (1994–2002): Implications for current kinematics of Asia, *Journal of Geophysical Research: Solid Earth*, **108**(B10).

Campanyà, J., Ledo, J., Queralt, P., Marcuello, A., & Jones, A. G., 2014. A new methodology to estimate magnetotelluric (MT) tensor relationships: Estimation of Local transfer-functIons by Combining Interstation Transfer-functions (ELICIT), *Geophysical Journal International*, **198**(1), 484–494.

Cashman, K. V. & Sparks, R. S. J., 2013. How volcanoes work: A 25 year perspective, *GSA bulletin*, **125**(5-6), 664–690.

Chen, M., Niu, F., Liu, Q., & Tromp, J., 2015. Mantle-driven uplift of Hangai Dome: New seismic constraints from adjoint tomography, *Geophysical Research Letters*, **42**(17), 6967–6974.

Cherevatova, M., Smirnov, M. Y., Korja, T., Pedersen, L. B., Ebbing, J., Gradmann, S., Becken, M., Group, M. W., et al., 2015. Electrical conductivity structure of north-west Fennoscandia from three-dimensional inversion of magnetotelluric data, *Tectonophysics*, **653**, 20–32.

Comeau, M., 2015. *Electrical Resistivity Structure of the Altiplano-Puna Magma Body and Volcan Uturuncu from Magnetotelluric Data: University of Alberta*, Ph.D. thesis, PhD thesis published by The University of Alberta Education and Research Archive, 337 pp.

Comeau, M. J., Unsworth, M. J., & Cordell, D., 2016. New constraints on the magma distribution and composition beneath Volcán Uturuncu and the southern Bolivian Altiplano from magnetotelluric data, *Geosphere*, **12**(5), 1391–1421.

Comeau, M. J., Becken, M., Käufl, J., Kuvshinov, A., Demberel, S., & the Hangai Working Group, 2018a. Images of intraplate volcanism: The upper crustal structure below Tariat volcanic zone, Mongolia, imaged with magnetotellurics, in *EGU General Assembly Conference Abstracts*, Vienna, Austria.

Comeau, M. J., Käufl, J., Becken, M., Kuvshinov, A., Grayver, A., Kamm, J., Demberel, S., Batmagnai, E., Tserendug, S., Eldev-Ochir, B., & Nasan-Ochir, T., 2018b. Electrical resistivity models reveal mineralization and fault systems in the Valley of the Lakes, south-central Mongolia, in *24th EM Induction Workshop Abstracts*, Helsingør, Denmark.

Comeau, M. J., Käufl, J. S., Becken, M., Kuvshinov, A., Grayver, A. V., Kamm, J., Demberel, S., Sukhbaatar, U., & Batmagnai, E., 2018c. Evidence for fluid and melt generation in response to an asthenospheric upwelling beneath the Hangai Dome, Mongolia, *Earth and Planetary Science Letters*, **487**, 201 – 209.

Comeau, M. J., Becken, M., Käufl, J., Grayver, A., Kuvshinov, A., Tserendug, S., Batmagnai, E., & Demberel, S., 2019. Evidence for terrane boundaries and suture zones across Southern Mongolia detected with a 2-dimensional magnetotelluric transect, Earth and Planetary Science Letters, in revision.

Connolly, J. & Podladchikov, Y. Y., 2013. A hydromechanical model for lower crustal fluid flow, in *Metasomatism and the chemical transformation of rock*, pp. 599–658, Springer.

Connolly, J. A. D. & Podladchikov, Y. Y., 2004. Fluid flow in compressive tectonic settings: Implications for midcrustal seismic reflectors and downward fluid migration, *Journal of Geophysical Research: Solid Earth*, **109**(B4).

Cunningham, W., 2001. Cenozoic normal faulting and regional doming in the southern Hangay region, Central Mongolia: implications for the origin of the Baikal rift province, *Tectonophysics*, **331**(4), 389–411.

Dmitriev, V. I., Il'inskii, A. S., & Sveshnikov, A. G., 1976. The developments of mathematical methods for the study of direct and inverse problems in electrodynamics, *Russian Mathematical Surveys*, **31**(6), 133.

Dong, H., Wei, W., Jin, S., Ye, G., Zhang, L., Jing, J., Yin, Y., Xie, C., & Jones, A. G., 2016. Extensional extrusion: Insights into south-eastward expansion of Tibetan Plateau from magnetotelluric array data, *Earth and Planetary Science Letters*, **454**, 78 – 85.

Egbert, G. D., 2002. Processing and interpretation of electromagnetic induction array data, *Surveys in geophysics*, **23**(2-3), 207–249.

828 Egbert, G. D. & Booker, J. R., 1986. Robust estimation of geomagnetic transfer functions,
829 *Geophysical Journal of the Royal Astronomical Society*, **87**(1), 173–194.
830 Ganbat, E. & Demberel, O., 2010. Geologic background of the Hangay geothermal system, west-
831 central Mongolia, in *Proceedings World Geothermal Congress*, p. 1e6.
832 García, X. & Jones, A. G., 2005. A new methodology for the acquisition and processing of
833 audio-magnetotelluric (AMT) data in the AMT dead band, *Geophysics*, **70**(5), G119–G126.
834 Grayver, A. V., 2015. Parallel three-dimensional magnetotelluric inversion using adaptive finite-
835 element method. Part I: theory and synthetic study, *Geophysical Journal International*, **202**(1),
836 584–603.
837 Grayver, A. V. & Kolev, T. V., 2015. Large-scale 3D geoelectromagnetic modeling using parallel
838 adaptive high-order finite element method, *Geophysics*, **80**(6), E277–E291.
839 Grayver, A. V. & Kuvshinov, A. V., 2016. Exploring equivalence domain in nonlinear inverse
840 problems using covariance matrix adaption evolution strategy (CMAES) and random sampling,
841 *Geophysical Journal International*, **205**(2), 971–987.
842 Guy, A., Schulmann, K., Janoušek, V., Štípská, P., Armstrong, R., Belousova, E., Dolgopolova,
843 A., Seltmann, R., Lexa, O., Jiang, Y., et al., 2015. Geophysical and geochemical nature of
844 relaminated arc-derived lower crust underneath oceanic domain in southern Mongolia, *Tectonics*,
845 **34**(5), 1030–1053.
846 Harpering, D., 2018. *Robust processing scheme for magnetotelluric data*, Master's thesis, WWU
847 Münster.
848 Harris, N., Hunt, A., Parkinson, I., Tindle, A., Yondon, M., & Hammond, S., 2010. Tectonic im-
849 plications of garnet-bearing mantle xenoliths exhumed by Quaternary magmatism in the Hangay
850 dome, central Mongolia, *Contributions to Mineralogy and Petrology*, **160**(1), 67–81.
851 Heise, W., Bibby, H. M., Caldwell, T. G., Bannister, S. C., Ogawa, Y., Takakura, S., & Uchida,
852 T., 2007. Melt distribution beneath a young continental rift: the Taupo Volcanic Zone, New
853 Zealand, *Geophysical Research Letters*, **34**(14).
854 Hermance, J. F. & Thayer, R. E., 1975. The telluric-magnetotelluric method, *Geophysics*, **40**(4),
855 664–668.
856 Hill, G. J., Bibby, H. M., Ogawa, Y., Wallin, E. L., Bennie, S. L., Caldwell, T. G., Keys, H.,
857 Bertrand, E. A., & Heise, W., 2015. Structure of the Tongariro Volcanic system: Insights from
858 magnetotelluric imaging, *Earth and Planetary Science Letters*, **432**, 115–125.
859 Hunt, A. C., Parkinson, I., Harris, N., Barry, T., Rogers, N., & Yondon, M., 2012. Cenozoic vol-
860 canism on the Hangai Dome, Central Mongolia: geochemical evidence for changing melt sources
861 and implications for mechanisms of melting, *Journal of Petrology*, **53**(9), 1913–1942.
862 Iliceto, V. & Santarato, G., 1986. On the possibility of the telluric method: some results on faulted

863 structures, *Geophysical prospecting*, **34**(7), 1082–1098.

864 Ionov, D., 2002. Mantle structure and rifting processes in the Baikal–Mongolia region: geophysical
865 data and evidence from xenoliths in volcanic rocks, *Tectonophysics*, **351**(1-2), 41–60.

866 Joshi, A., Bangerth, W., & Sevick-Muraca, E. M., 2004. Adaptive finite element based tomography
867 for fluorescence optical imaging in tissue, *Optics Express*, **12**(22), 5402–5417.

868 Karypis, G. & Kumar, V., 1999. A fast and highly quality multilevel scheme for partitioning
869 irregular graphs, *Journal on Scientific Computing*, **20**(1), 359–392.

870 Käufl, J. S., Grayver, A. V., & Kuvshinov, A. V., 2018. Topographic distortions of magnetotelluric
871 transfer functions: a high-resolution 3-d modelling study using real elevation data, *Geophysical*
872 *Journal International*, **215**(3), 1943–1961.

873 Kay, R. W. & Kay, S. M., 1993. Delamination and delamination magmatism, *Tectonophysics*,
874 **219**(1-3), 177–189.

875 Khoza, T. D., Jones, A. G., Muller, M. R., Evans, R. L., Miensopust, M. P., & Webb, S. J., 2013.
876 Lithospheric structure of an Archean craton and adjacent mobile belt revealed from 2-D and 3-D
877 inversion of magnetotelluric data: Example from southern Congo craton in northern Namibia,
878 *Journal of Geophysical Research: Solid Earth*, **118**(8), 4378–4397.

879 Krystopowicz, N. J. & Currie, C. A., 2013. Crustal eclogitization and lithosphere delamination
880 in orogens, *Earth and Planetary Science Letters*, **361**, 195–207.

881 Liu, L. & Hasterok, D., 2016. High-resolution lithosphere viscosity and dynamics revealed by
882 magnetotelluric imaging, *Science*, **353**(6307), 1515–1519.

883 Manning, C. E., 2018. Fluids of the lower crust: deep is different, *Annual Review of Earth and*
884 *Planetary Sciences*, **46**, 67–97.

885 McDannell, K. T., Zeitler, P. K., & Idleman, B. D., 2018. Relict topography within the Hangay
886 Mountains in central Mongolia: Quantifying long-term exhumation and relief change in an old
887 landscape, *Tectonics*, **37**(8), 2531–2558.

888 Meissner, R. & Mooney, W., 1998. Weakness of the lower continental crust: a condition for
889 delamination, uplift, and escape, *Tectonophysics*, **296**(1-2), 47–60.

890 Melosh, G., Cumming, W., Benoit, D., Wilmarth, M., Colvin, A., Winick, J., Soto-Neira, E.,
891 Sussman, D., Urzúa-Monsalve, L., Powell, T., et al., 2010. Exploration results and resource
892 conceptual model of the Tolhuaca geothermal field, Chile, in *Proceedings, World Geothermal*
893 *Congress*.

894 Meltzer, A., Stachnik, J. C., Sodnomsambuu, D., Munkhuu, U., Tsagaan, B., Dashdondog, M., &
895 Russo, R., 2019. The Central Mongolia Seismic Experiment: Multiple Applications of Temporary
896 Broadband Seismic Arrays, *Seismological Research Letters*, **90**(3), 1364–1376.

897 Meqbel, N. M., Egbert, G. D., Wannamaker, P. E., Kelbert, A., & Schultz, A., 2014. Deep

electrical resistivity structure of the northwestern US derived from 3-D inversion of USArray magnetotelluric data, *Earth and Planetary Science Letters*, **402**, 290–304.

Miensopust, M. P., 2017. Application of 3-D electromagnetic inversion in practice: Challenges, pitfalls and solution approaches, *Surveys in Geophysics*, **38**(5), 869–933.

Muñoz, G., 2014. Exploring for geothermal resources with electromagnetic methods, *Surveys in geophysics*, **35**(1), 101–122.

Murphy, B. S. & Egbert, G. D., 2017. Electrical conductivity structure of southeastern North America: implications for lithospheric architecture and Appalachian topographic rejuvenation, *Earth and Planetary Science Letters*, **462**, 66–75.

NASA JPL, 2013. NASA Shuttle Radar Topography Mission Global 1 arc second. NASA LP DAAC, https://doi.org/10.5067/MEaSUREs/SRTM/SRTMGL1.003.

Nieuwenhuis, G., Unsworth, M. J., Pana, D., Craven, J., & Bertrand, E., 2014. Three-dimensional resistivity structure of Southern Alberta, Canada: implications for Precambrian tectonics, *Geophysical Journal International*, **197**(2), 838–859.

Oyuntsetseg, D., Ganchimeg, D., Minjigmaa, A., Ueda, A., & Kusakabe, M., 2015. Isotopic and chemical studies of hot and cold springs in western part of Khangai Mountain region, Mongolia, for geothermal exploration, *Geothermics*, **53**, 488–497.

Peacock, J. R., Mangan, M. T., McPhee, D., & Wannamaker, P. E., 2016. Three-dimensional electrical resistivity model of the hydrothermal system in Long Valley Caldera, California, from magnetotellurics, *Geophysical Research Letters*, **43**(15), 7953–7962.

Petit, C., Tiberi, C., Deschamps, A., & Déverchère, J., 2008. Teleseismic traveltimes, topography and the lithospheric structure across central Mongolia, *Geophysical Research Letters*, **35**(11).

Platz, A. & Weckmann, U., 2019. An automated new pre-selection tool for noisy Magnetotelluric data using the Mahalanobis distance and magnetic field constraints, *Geophysical Journal International*.

Priestley, K., Debayle, E., McKenzie, D., & Pilidou, S., 2006. Upper mantle structure of eastern Asia from multimode surface waveform tomography, *Journal of Geophysical Research: Solid Earth*, **111**(B10).

Rikitake, T., 1948. Notes on electromagnetic induction within the Earth, *Bull. Earthq. Res. Inst*, **24**(1), 4.

Rizza, M., Ritz, J.-F., Prentice, C., Vassallo, R., Braucher, R., Larroque, C., Arzhannikova, A., Arzhannikov, S., Mahan, S., Massault, M., et al., 2015. Earthquake geology of the Bulnay fault (Mongolia), *Bulletin of the Seismological Society of America*, **105**(1), 72–93.

Robertson, K., Heinson, G., & Thiel, S., 2016. Lithospheric reworking at the Proterozoic-Phanerozoic transition of Australia imaged using AusLAMP Magnetotelluric data, *Earth and*

Planetary Science Letters, **452**, 27 – 35.

Robertson, K., Heinson, G., Taylor, D., & Thiel, S., 2017. The lithospheric transition between the Delamerian and Lachlan orogens in western Victoria: new insights from 3D magnetotelluric imaging, *Australian Journal of Earth Sciences*, **64**(3), 385–399.

Rousseeuw, P. J., 1984. Least median of squares regression, *Journal of the American Statistical Association*, **79**(388), 871–880.

Rung-Arunwan, T., Siripunvaraporn, W., & Utada, H., 2016. On the Berdichevsky average, *Physics of the Earth and Planetary Interiors*, **253**, 1 – 4.

Sahagian, D., Proussevitch, A., Ancuta, L., Idleman, B., & Zeitler, P., 2016. Uplift of Central Mongolia recorded in vesicular basalts, *The Journal of Geology*, **124**(4), 435–445.

Samrock, F., Grayver, A. V., Eysteinsson, H., & Saar, M. O., 2018. Magnetotelluric image of transcrustal magmatic system beneath the Tulu Moye geothermal prospect in the Ethiopian rift, *Geophysical Research Letters*, **45**(23), 12–847.

Styron, R., 2018. GEM global active faults, http://doi.org/10.5281/zenodo.1404388.

Tiberi, C., Deschamps, A., Déverchère, J., Petit, C., Perrot, J., Appriou, D., Mordvinova, V., Dugaarma, T., Ulzibaat, M., & Artemiev, A., 2008. Asthenospheric imprints on the lithosphere in central Mongolia and southern Siberia from a joint inversion of gravity and seismology (MOBAL experiment), *Geophysical Journal International*, **175**(3), 1283–1297.

Tietze, K. & Ritter, O., 2013. Three-dimensional magnetotelluric inversion in practice-the electrical conductivity structure of the San Andreas Fault in Central California, *Geophysical Journal International*, **195**(1), 130–147.

Tikhonov, A., 1950. On determining electrical characteristics of the deep layers of the Earths crust, in *Doklady*, vol. 73, pp. 295–297, Citeseer.

Tikhonov, A. N., 1963. On the solution of ill-posed problems and the method of regularization, in *Doklady Akademii Nauk*, vol. 151, pp. 501–504, Russian Academy of Sciences.

Unsworth, M. & Bedrosian, P. A., 2004. Electrical resistivity structure at the SAFOD site from magnetotelluric exploration, *Geophysical Research Letters*, **31**(12).

Usui, Y., Ogawa, Y., Aizawa, K., Kanda, W., Hashimoto, T., Koyama, T., Yamaya, Y., & Kagiyama, T., 2016. Three-dimensional resistivity structure of Asama volcano revealed by data-space magnetotelluric inversion using unstructured tetrahedral elements, *Geophysical Journal International*, **208**(3), 1359–1372.

Van der Voo, R., van Hinsbergen, D. J., Domeier, M., Spakman, W., & Torsvik, T. H., 2015. Latest Jurassic–earliest Cretaceous closure of the Mongol-Okhotsk Ocean: A paleomagnetic and seismological-tomographic analysis, *Geological Society of America Special Papers*, **513**, 589–606.

Vergnolle, M., Pollitz, F., & Calais, E., 2003. Constraints on the viscosity of the continental crust

968 and mantle from GPS measurements and postseismic deformation models in western Mongolia,
969 *Journal of Geophysical Research: Solid Earth*, **108**(B10).
970 Walker, R., Nissen, E., Molor, E., & Bayasgalan, A., 2007. Reinterpretation of the active faulting
971 in central Mongolia, *Geology*, **35**(8), 759–762.
972 Walker, R., Molor, E., Fox, M., & Bayasgalan, A., 2008. Active tectonics of an apparently aseis-
973 mic region: distributed active strike-slip faulting in the Hangay Mountains of central Mongolia,
974 *Geophysical Journal International*, **174**(3), 1121–1137.
975 Weidelt, P., 1972. The inverse problem of geomagnetic induction, *J. Geophys.*, **38**, 257–289.
976 Windley, B. F. & Allen, M. B., 1993. Mongolian plateau: Evidence for a late Cenozoic mantle
977 plume under central Asia, *Geology*, **21**(4), 295–298.
978 Xu, S., Unsworth, M. J., Hu, X., & Mooney, W. D., 2019. Magnetotelluric evidence for asym-
979 metric simple shear extension and lithospheric thinning in south China, *Journal of Geophysical*
980 *Research: Solid Earth*, **124**(1), 104–124.
981 Yang, B., Egbert, G. D., Kelbert, A., & Meqbel, N. M., 2015. Three-dimensional electrical
982 resistivity of the north-central USA from EarthScope long period magnetotelluric data, *Earth*
983 *and Planetary Science Letters*, **422**, 87 – 93.
984 Yoshino, T., Matsuzaki, T., Shatskiy, A., & Katsura, T., 2009. The effect of water on the electrical
985 conductivity of olivine aggregates and its implications for the electrical structure of the upper
986 mantle, *Earth and Planetary Science Letters*, **288**(1), 291 – 300.
987 Yungul, S. H., 1977. The telluric methods in the study of sedimentary structures-a survey, *Geo-*
988 *exploration*, **15**(4), 207–238.
989 Zhang, F., Wu, Q., Grand, S. P., Li, Y., Gao, M., Demberel, S., Ulziibat, M., & Sukhbaatar, U.,
990 2017. Seismic velocity variations beneath central Mongolia: Evidence for upper mantle plumes?,
991 *Earth and Planetary Science Letters*, **459**, 406–416.